Potential Vorticity Generation by West African Squall Lines

Richard H. Johnson*, and Paul E. Ciesielski

Department of Atmospheric Science, Colorado State University, Fort Collins, Colorado

**Corresponding author address:* Richard H. Johnson, Department of Atmospheric Science, 1371 Campus Delivery, Colorado State University, Fort Collins, CO 80523.

E-mail: Richard.H.Johnson@colostate.edu

ABSTRACT

The West African summer monsoon features multiple, complex interactions between African Easterly Waves (AEWs), moist convection, variable land surface properties, dust aerosols, and the diurnal cycle. One aspect of these interactions, the coupling between convection and AEWs, is explored using observations obtained during the 2006 African Monsoon Multidisciplinary Analyses (AMMA) field campaign. During AMMA, research weather radar operated at Niamey, Niger, where it intercepted 28 squall line systems characterized by leading convective lines and trailing stratiform regions. Nieto Ferreira et al. found that the squall lines were linked with the passage of AEWs and classified them into two tracks, northerly and southerly, based on the position of the African Easterly Jet (AEJ). Using AMMA sounding data, a composite of northerly squall lines that tracked on the cyclonic shear side of the African Easterly Jet (AEJ) is created. Latent heating within the trailing stratiform regions produced a mid-tropospheric positive potential vorticity (PV) anomaly centered at the melting level, as commonly observed in such systems. However, a unique aspect of these PV anomalies is that they combined with a 400-500 hPa positive PV anomaly extending southward from the Sahara. The latter feature is a consequence of the deep convective boundary layer over the hot Saharan desert. Results provide evidence of a coupling and merging of two PV sources – one associated with the Saharan heat low and another with latent heating – that ends up creating a prominent mid-tropospheric positive PV maximum to the rear of West African squall lines.

1. Introduction

The dominant rain producers over West Africa during the summer monsoon are westward-moving squall lines consisting of leading convective lines and trailing stratiform precipitation regions (Hamilton and Archbold 1945; Aspliden et al. 1976; Houze 1977; Roux et al. 1984; Chong et al. 1987; Chalon et al. 1988; Roux 1988). The squall lines are commonly associated with African Easterly Waves (AEWs; e.g., Carlson 1969; Burpee 1974; Reed et al. 1977; Kiladis et al. 2006), which propagate along the African Easterly Jet (AEJ). They typically possess two circulation centers or vorticity maxima: one at the level of the AEJ (600-700 hPa) just south of the jet axis and the other at lower levels to the north of the axis along the baroclinic zone at the southern edge of the Saharan heat low (e.g., Reed et al. 1977; Thorncroft and Hodges 2001).

The relationship of convection to AEWs is complex and varies from land to ocean. South of the AEJ axis over land, convection typically leads the AEW trough, while to the north of the AEJ convection is positioned in the southerly flow to the rear of the trough axis (e.g., Duvel 1990; Fink and Reiner 2003; Kiladis et al. 2006). While these phase relationships between convection and AEWs have been widely documented, mechanisms involving the coupling between the diabatic processes in the convective systems and AEW dynamics are not yet fully understood. For convection south of the AEJ, studies have shown that low-level convergence ahead of the trough axis contributes to convection developing there (e.g., Carlson 1969; Payne and McGarry 1977; Reed et al. 1977; Fink and Reiner 2003; Tomassini 2018). The resultant latent heating in the convective systems has been implicated in the intensification of the AEWs (Norquist et al. 1977; Berry and Thorncroft 2005, 2012; Hsieh and Cook 2007, 2008; Tomassini et al. 2017). However, given that the response of the large-scale environment to latent heating depends critically on its vertical profile (e.g., Hartmann et al. 1984; Schumacher et al. 2004) and that the precipitation characteristics

(e.g., convective/stratiform ratios) of convective systems vary greatly over West Africa (Schumacher and Houze 2006; Guy et al. 2011), significant regional differences in convection-AEW interactions likely exist.

The vertical profile of latent heating in convective systems has a significant impact on the potential vorticity (PV) field (Schubert et al. 1989; Raymond and Jiang 1990). As shown by Hertenstein and Schubert (1991), there are differing responses to latent heating in the convective line and stratiform region of squall lines. The convective line latent heating that peaks in the mid-troposphere produces a positive PV anomaly at low levels and negative anomaly in the upper troposphere. On the other hand, the stratiform region with heating aloft and cooling at low levels generates a positive PV anomaly in the mid-troposphere. While the importance of the background PV field in AEW development has long been recognized (Burpee 1972), the specific impact of the vertical distribution of latent heating on the dynamics of AEWs has been more recently explored using reanalyses and numerical simulations (Hsieh and Cook 2008; Berry and Thorncroft 2012; Janiga and Thorncroft 2013; Tomassini et al. 2017; Tomassini 2018). This study is intended to add to those previous works with a more observationally based approach.

Observations taken during the summer 2006 African Monsoon Multidisciplinary Analyses (AMMA; Redelsperger et al. 2006) field campaign are used, with particular attention to the latent heating and circulation characteristics of squall line systems. Over two dozen West African squall lines were sampled during AMMA by the MIT C-band weather radar located near Niamey, Niger (13.5°N, 2.2°E). Using the MIT radar observations, the structural characteristics and the diurnal behavior of the squall lines, as well as their relationship to African Easterly Waves (AEWs) were analyzed by Rickenbach et al. (2009); Nieto Ferreira et al. (2009); Guy et al. (2011). The results of these studies are incorporated into our investigation.

In addition to the radar observations at Niamey, a special sounding network was established over West Africa to document the the environmental conditions associated with the AEWs and convective systems that move through the region (Parker et al. 2008). Both the radar observations and analyses from the sounding network are combined to determine the structure and latent heating characteristics of the squall lines and how they might impact AEWs over west central Africa. The advantage of using analyses from the core sounding network is that unlike in the case of reanalysis datasets and numerical modeling, diagnosed fields such as the divergence profiles are independent of model parameterizations.

2. Data and Methods

a. Sounding observations

The analysis here is based on the dataset collected during the AMMA Special Observing Period (SOP; defined here as June to September 2006) over the area shown in Fig. 1. During this period some 7,000 upper-air soundings were taken, representing the greatest density of radiosondes ever launched over this region (Parker et al. 2008). The observations centered around six core sounding sites which formed the adjacent quadrilateral and triangular networks seen in Fig. 1 and allow for north-south analysis transects over this region. Hereafter, these two networks will be referred to as the Northern and Southern Enhanced Budget Arrays (EBAN and EBAS, respectively). EBAN extends into a portion of the Sahel. Sounding observations were conducted at these core sites with 2-4 day^{-1} frequency during much the SOP and 8 day^{-1} during two intensive observing periods (IOPs; 20-29 June 2006 and 1-15 August 2006). These IOPs were intended to capture pre-monsoon and monsoon conditions, respectively, within this region. A visual inventory of the

sounding data at the core sites and a discussion of the humidity corrections made to the data can be found in the Appendix.

b. Gridded analysis procedure

Data used in the production of the gridded analyses included 6,600 upsondes (the vast majority of which were at high vertical resolution) from 27 land sites and 12 research vessels, 558 dropsondes from two aircraft, 109 driftsondes (Cohn et al. 2013), 733 pibal soundings from 14 sites (Parker et al. 2008), and 1,270 3-h averaged wind profiles from three wind profilers located in the vicinity of the core sites (Fig. 1). While pibal winds were confined to the lowest few kilometers, profiler winds were generally present up to 6 km. Additional quality controls were applied to all soundings as described in Ciesielski et al. (2012).

To supplement these data sources, 6-h analysis fields from a special AMMA ECMWF reanalysis (Agustí-Panareda et al. 2010) were used at 5° grid intersections if no observations were present within a 3° radius. Key features of this reanalysis include use of a new model version with improved physics, inclusion of all high vertical resolution AMMA radiosonde data, and implementation of a rawinsonde humidity-bias correction method as described in Agustí-Panareda et al. (2009). The main impact of using this reanalysis is over the data-void regions outside the core arrays (e.g., over the oceans), except for periods when radiosonde data at a core site did not exist for whatever reason (data gaps depicted Fig. A1). When soundings from all core sites were present, fields within the enhanced networks are largely independent of the model analyses and hence their physical parameterizations, which makes this study distinct from those relying on reanalysis fields.

The quality-controlled sounding data, along with the other data sources and reanalysis described above, were objectively analyzed onto a $1^\circ \times 1^\circ$ grid at 6-h intervals for the SOP and at 3-h intervals for the IOPs. Using multiquadric interpolation (Nuss and Titley 1994), gridded analyses

of the basic fields were produced at the surface and at 25-hPa intervals from 1000 to 50 hPa over the large-scale sounding array (LSA) from 20°W to 20°E and the equator to 20°N. The divergence field was mass balanced in the vertical by assuming adiabatic flow at the tropopause level (typically around 100 hPa), which was determined at each grid point and each time interval. In an effort to assess the reliability of the divergence estimates from the sounding network, precipitation estimates based on the moisture budget are compared to Tropical Rainfall Measuring Mission (TRMM) 3B42 estimates. Despite complications in budget estimates due to the coarseness of the sounding network, topographic effects, uncertainties in estimates of surface evaporation over land, and uncertainties in TRMM 3B42 precipitation over land, there is reasonable agreement between the independent estimates (Appendix).

c. MIT radar observations

The MIT C-band radar operated at Niamey (13.5°N, 2.2°E) during the period 5 July to 27 September (Nieto Ferreira et al. 2009; Rickenbach et al. 2009; Guy et al. 2011) taking 3-D reflectivity volumes to a range of 150 km every 10 min. The principal focus of this study is the placement of the sounding data in the context of the observations from the MIT radar site, which is situated at the corner of the two sounding array polygons EBAN and EBAS (Fig. 1). The radar sampling area (Fig. 1) is considerably smaller than the sounding array areas so the sounding network is unable to resolve convective-scale features of the storms passing through the radar domain. Several aspects of the radar analyses will be utilized. First, convective/stratiform partitioning data based on the MIT radar (Nieto Ferreira et al. 2009; Guy et al. 2011) will be incorporated into our study. Second, information about individual squall lines that passed the radar site (Nieto Ferreira et al. 2009; Rickenbach et al. 2009) will be used to investigate mesoscale aspects of the squall systems through a compositing analysis.

During the MIT radar deployment at Niamey, 28 squall lines were observed to pass the radar site (Nieto Ferreira et al. 2009). Rickenbach et al. (2009) found that 20 of the 28 squall lines arrived at the Niamey radar site during the early morning, having originated the previous afternoon over elevated terrain, principally the Jos Plateau, ∼800 km to the southeast. They found the diurnal cycle of rainfall to be bimodal, with a primary maximum related to the nocturnal squall line passage and a secondary peak associated with afternoon isolated convection. Squall lines were the most important rain producers during the period of radar operation, contributing 82% of the total rainfall despite being present only 17% of the time (Nieto Ferreira et al. 2009). Given this, sounding-based diagnosed properties of convection in the region can be expected to primarily reflect those associated with squall line systems, which are characterized over West Africa by leading convective lines and trailing stratiform regions (e.g., Hamilton and Archbold 1945; Aspliden et al. 1976; Houze 1977; Chong et al. 1987; Roux 1988). Cetrone and Houze (2011) investigated the non-precipitating anvil characteristics of 15 squall lines that passed the radar site during AMMA, all of which had leading-line/trailing-stratiform precipitation structures.

Out of the 28 cases examined in Nieto Ferreira et al. (2009), a selection of 12 (shown in Table 1) has been made that had the largest dimension and were best sampled by the MIT radar based on a perusal of sequences of PPI images. Radar depictions of two of the squall lines selected are shown in Fig. 2. Each of the two moved from east to west and had a leading convective line oriented in an approximately north-south direction with a trailing stratiform precipitation system separated from the convective line by a weak-reflectivity transition zone. To a greater or lesser degree, all cases had a leading-line/trailing-stratiform (LL/TS) structure and the majority of the 12 cases had an approximately north-south orientation (Table 1). Also identified in Table 1 is a classification of the squall lines as to whether they were associated with the passage of northerly or southerly African easterly wave (AEW) tracks according to Nieto Ferreira et al. (2009). Results pertaining

to this classification will be presented later. Ten of the 12 squall line passages occurred during the morning hours, while two were in the mid-afternoon. The squall line speeds ranged from 10 to 25 m s^{-1}, with an average speed of 17.2 m s^{-1}.

Composite analyses of the 12 cases have been created by assigning a time scale to the squall line passage determined by the time at which the center of the convective lines for each case passed the MIT radar site. Those times are indicated in Table 1. To illustrate the LL/TS characteristics of the composited cases, time series of rainfall rate, stratiform rain fraction, and stratiform rain area relative to squall line passage for these cases have been determined (Fig. 3). Values shown are averages over a 20 km $\times$ 20 km area centered at the radar site. Both conditional rain rate (average rain rate over areas where it is raining) and unconditional rain rate (average rain rate over entire 20 km $\times$ 20 km area) peak near t=0, corresponding to minima in stratiform fraction and stratiform area. Over a period of 3-4 h following passage, the stratiform fraction and area increased, reaching nearly 100% at t= +4 h. The overall evolution of the precipitation fields in Fig. 3 is consistent with the passage of an LL/TS squall system (Houze 1977; Zipser 1977; Chong et al. 1987; Roux 1988).

d. Other data sources

Surface meteorological observations at 1-min intervals from the Atmospheric Radiation Measurement (ARM) mobile facility located at the Niamey airport (Miller and Slingo 2007) are used to document the passage of squall lines. Surface fluxes were also available at this site; however, they are not necessarily representative of the larger domain, so ECMWF reanalysis fluxes are used in the study. Reanalysis flux biases are discussed in detail in Agustí-Panareda et al. (2010).

Cloud parameters and column-net radiative heating rates (Q_R) are obtained from the Clouds and the Earth's Radiant Energy System (CERES) product at 3-h intervals on a 1° grid (Wielicki

et al. 1996). High vertical resolution (681 levels) profiles of Q_R at 2-min resolution were available for the period from 1 July to 30 September 2006 based on radiative transfer calculations and observations from the ARM mobile facility at Niamey (Powell et al. 2012). The mean diurnal cycle of radiative heating for this 3-month period was used to fill in missing times (June 1-30, and July 21-22) and bad data (heating rates with a 3σ departure from the diurnal mean). To obtain radiative heating profiles over the budget arrays, the vertical profiles of Q_R were averaged in 3-h bins then adjusted by a constant fraction at each level so that its vertical integral matched that of the CERES product averaged over the arrays.

Rainfall rates derived from the sounding budget are compared to estimates from the TRMM 3B42v7 product. This TRMM product is available at 3-h, $0.25^\circ \times 0.25^\circ$ resolution by combining microwave rainfall estimates from TRMM and other satellites with high temporal infrared rain estimates and with surface gauge data where available (Huffman et al. 2007).

3. Results

a. Conditions over sounding arrays prior to and following monsoon onset

The main focus of this study is on the properties of convection within the region of the sounding arrays EBAN and EBAS. A map of June through September mean rainfall over the LSA is shown in Fig. 4. Rainfall maxima were observed to the west or windward side (with respect to the southwesterly low-level monsoon flow) of several prominent terrain features over West Africa – the Guinea Highlands, the Jos Plateau, and the Cameroon Highlands. Minor rainfall maxima also occurred over higher terrain within the EBAS and EBAN. Past studies have demonstrated the importance of terrain features in generating localized convective systems and squall lines in their proximity in the afternoon, followed by subsequent westward propagation in the easterly flow aloft

(Rowell and Milford 1993; Hodges and Thorncroft 1997; Fink and Reiner 2003; Mohr 2004; Fink et al. 2006; Laing et al. 2008; Rickenbach et al. 2009; Janiga and Thorncroft 2014). Because of its location just east of the EBAS and EBAN, one of these features, the Jos Plateau, influences the timing of convection passing over the arrays (Fink et al. 2006), which explains the frequently observed nighttime/early-morning arrival of squall lines at the MIT radar site (Nieto Ferreira et al. 2009; Rickenbach et al. 2009; Guy et al. 2011).

While Fig. 4 depicts the rainfall distribution over the entire LSA, the north-south variation of rainfall from the equator to 20°N over a smaller region that includes the longitudes of the sounding arrays (0-7°E) is shown in Fig. 5. The range of longitudes for Fig. 5 and subsequent analyses of meridional variations was selected because it contains the highest density of sounding observations, namely, those comprising EBAS and EBAN (Fig. 1). Included in this figure is the 500-hPa vertical p-velocity ω based on the gridded analyses. Overall, there is good agreement between the peaks in rainfall and mid-tropospheric upward motion maxima, lending credence to the ability of the sounding network to capture realistic estimates of vertical profiles of divergence (see Appendix for more detailed analysis). In a review of the AMMA field campaign, Janicot et al. (2008) reported that convective activity over the Sahel began around 10 July, delayed from its normal onset date by 10 days possibly due to the passage of an MJO around that time. Using 10 July as monsoon onset date for the EBAN, which extends into the Sahel, pre-monsoon and monsoon periods defined in subsequent analyses are denoted in Fig. 5. This definition of pre-monsoon period, whose beginning on 1 June is based on the initial operation of the sounding network, differs from the preonset period of the West African monsoon defined by Sultan and Janicot (2003), which climatologically begins in mid-May and ends in late June. Prior to monsoon onset, maxima in rainfall and upward motion were generally confined to 2-6°N, while following onset, rainfall and

vertical motion peaks shifted northward and extended over a much broader latitude range, from $\sim$5° to 15°N.

The northward advance of the summer monsoon is illustrated in vertical cross sections of the meridional wind v and specific humidity q (Fig. 6). Following onset, moisture and rainfall shift northward while drying and reduced rainfall are observed at the equator. The low-level southerly flow intensified somewhat near 10°N after onset but not by a significant amount. Lothon et al. (2008) showed that throughout the AMMA SOP low-level southerly flow (a nocturnal low-level jet) peaked at 400 m above ground level in the early morning hours with an accompanying maximum northward moisture transport at that time. Associated with the poleward advance of moisture after onset is a significant reduction in cloud-base height poleward of 10°N (e.g., Lafore et al. 2011).

Vertical cross sections of the zonal wind and absolute vorticity before and after monsoon onset are shown in Figs. 7a,b. From pre-monsoon to monsoon the average AEJ at 600 hPa shifted from 10°N to 15°N, as reported in Janicot et al. (2008). Accompanying this transition was a reversal in the north-south gradient of absolute vorticity (color), indicating the necessary condition for barotropic instability of the mean zonal flow existed between 700 and 400 hPa (Burpee 1972; Reed et al. 1977). A tongue of high potential vorticity (PV = $\frac{1}{\rho}\boldsymbol{\zeta}_a \cdot \nabla\theta$; where ρ is density; $\boldsymbol{\zeta}_a$ the absolute vorticity vector, and θ potential temperature), is seen in the 400-500 hPa layer extending equatorward from 20°N and broadening after monsoon onset (Figs. 7c,d).[1] This high-PV feature, originally reported by Burpee (1972), is associated with a layer of high static stability atop a near-neutral layer over the Sahara that is a result of exceptionally deep convective boundary layers over the intensely heated desert surface (Karyampudi and Carlson 1988; Cuesta et al. 2009; Messager

[1] Viewed at a lower level (700 hPa; Fig. 7d), the PV maximum near 10°N is part of a long strip of high PV extending across West Africa on the cyclonic shear side of the AEJ (Berry and Thorncroft 2005; Janiga and Thorncroft 2013).

et al. 2010; Garcia-Carreras et al. 2015; Tomassini 2018). This stable layer is strengthened by shortwave radiative heating of the dust that is lofted from the surface to the top of the mixed layer or Saharan Air Layer (SAL: Carlson and Prospero 1972; Karyampudi and Carlson 1988). In the same way that the trade inversion in the subtropics has been shown to be dynamically extended along isentropes into the deep tropics (Schubert et al. 1995), the layer of high stability atop the heated Saharan boundary layer extends equatorward along isentropes (Figs. 7c,d) and then links up with the PV maximum on the equatorward side of the AEJ. This mean PV distribution closely resembles that reported by Janiga and Thorncroft (2013) within the longitude range 0-10°W for July-September 1998-2009 based on ERA-Interim data.

Also depicted in Figs. 7c,d are regions of reversed north-south gradient of PV along isentropic surfaces (stippling), an indication of the possibility of barotropic-baroclinic instability of the zonal flow (Charney and Stern 1962; Eliassen 1983). Prior to monsoon onset, there is a reversal of the PV gradient poleward of 7°N and below 600 hPa (Fig. 8c); however, this layer deepened after onset (Fig. 7d). In addition, there is region of reversed PV gradient in the upper troposphere, particularly prominent after monsoon onset. Diedhiou et al. (2002) associate this feature with the upper-tropospheric Tropical Easterly Jet (TEJ), which extends from the Asia Subcontinent westward across Africa. Schubert et al. (1991) argue that convection associated with the ITCZ alone is sufficient to generate these two PV gradient reversals, the lower one poleward and the upper one equatorward of the rainfall maximum. The rainfall distributions during AMMA (lower panels in Fig. 7) are generally consistent with this concept. Schubert et al. (1991) also propose that ITCZ convection by itself can account for instability of the lower-tropospheric easterly jet, not requiring strong heating over the Sahara. The low values of PV near the Sahara (Figs. 7c,d), however, are clearly associated with the deep convective boundary layers there reflected in the nearly constant θ below 600 hPa (Thorncroft and Blackburn 1999; Dickinson and Molinari 2000),

which serve to amplify the PV gradient reversal (Karyampudi and Pierce 2002; Hsieh and Cook 2008). The high values of PV related to the SAL are argued to be important in the amplification of AEWs as well as subsequent tropical cyclogenesis (Jones et al. 2004; Tomassini 2018).

Next shown are vertical cross sections of divergence and relative humidity before and after monsoon onset (Figs. 8a,b). Accompanying the northward advance and overall increase in rainfall over the region (lower panels, Fig. 8) is a northward push, broadening, and increase in both moisture throughout the column and upper-level divergence. In addition to the moistening at low and upper levels, a broad area of moistening is observed near the 0°C level (∼580 hPa), reflecting the prevalence of stratiform precipitation associated with the common squall line passages in the region (Chong et al. 1987; Roux 1988; Nieto Ferreira et al. 2009; Rickenbach et al. 2009; Guy et al. 2011) and the saturated conditions at the bases of the stratiform anvil clouds (Leary and Houze 1979). Convergence near the melting layer (Mapes and Houze 1995; Johnson et al. 1996) expands and extends northward following onset. Prior to onset, a shallow, dry circulation characterized by low-level convergence and divergence near 600 hPa is observed to the north in proximity to the Saharan heat low.

Using the gridded sounding dataset, the apparent heat source Q_1 (Yanai et al. 1973) over the longitudes of the sounding array areas has been computed. North-south cross sections of Q_1, vertical p-velocity (ω) before and after onset are shown in Figs. 8c,d. Prior to onset, there was a peak in Q_1 near 500 hPa (Fig. 8c) centered near the rainfall maximum around 5°N. The peak intensified and shifted upward after onset, as well as moving northward, corresponding to an overall increase and northward shift of rainfall (Fig. 8, lower panels). Strong upward motion at low levels capped by subsidence aloft existed over the Sahel prior to onset (Fig. 8c), but the upward motion weakened after onset as precipitation encroached into the region. Large positive values of Q_1 near the surface at northerly latitudes before and after onset are associated with boundary layer

turbulent fluxes over the strongly heated terrain. The north-south distributions of Q_1 are broadly similar to those determined from ERA-Interim data for June-September 1998-2007 in the AEW composite study of Poan et al. (2014).

b. Diagnosed properties of convection based on radar convective-stratiform partitioning

Using MIT radar convective/stratiform precipitation data provided by Nick Guy (2010, personal communication) an average 56% stratiform rainfall fraction (SF) in the radar domain has been determined for the entire period of AMMA operation. Dividing sounding-network-based heat and moisture budgets computed at 6-h intervals into two groups, one for SF greater than 56% and one for SF less than 56% (with average values of SF of 82% and 30%, and comprising 98 and 102 cases, respectively), and averaging over a region downscaled to the 150-km radius domain of the radar yields the results shown in Fig. 9. Profiles of the radiative heating rate Q_R are slightly different for high and low SF. The profile for high SF is consistent with the idea that stratiform clouds trailing squall lines have their bases near the 0°C level (Leary and Houze 1979) and in such systems longwave heating occurs near their bases and cooling near their tops (Webster and Stephens 1980). Such a configuration has a destabilizing influence on the trailing stratiform systems. Referring next to the profiles of convective heating $Q_1 - Q_R$, it can be seen that the profiles for both high and low SF are nearly identical (Fig. 9a), seemingly an unexpected result. From previous studies, one would expect high-SF $Q_1 - Q_R$ profiles to be positive aloft and negative at low levels while low SF profiles would be expected to be bottom-heavy (e.g., Houze 1982; Johnson 1984; Schumacher et al. 2004). However, both categories exhibit similarly shaped, top-heavy profiles, indicative of the combined effects of convective and stratiform precipitation in squall-type systems ((e.g., Houze 1982; Johnson 1984; Mapes and Houze 1995). The explanation for this apparent discrepancy is that the MIT radar domain area is so much smaller than the sounding array areas (Fig.

1) that it is not possible to resolve convective/stratiform variability over the radar domain, hence only the aggregate properties of the entire convective systems are diagnosed when scaled down to the radar area.

While the $Q_1 - Q_R$ profiles are nearly identical, the Q_2 profiles for high and low SF are distinctly different (Fig. 9b). Although the same line of reasoning above for the similarly shaped $Q_1 - Q_R$ profiles would seem to apply to the Q_2 profiles, that does not appear to be the case. The explanation may lie in the fact that the mid-to-upper troposphere for low SF is considerably drier than for high SF (Fig. 9c), which argues for increased evaporation in these layers for those cases. The atmosphere may even be locally drier just preceding the leading convective lines of squall systems due to the fact that the majority occurred in the dry northerly flow in advance of the AEW troughs as they passed the longitude of the radar domain (Nieto Ferreira et al. 2009). The resulting profiles of the vertical flux of moist static energy F (Fig. 9d), proportional to the vertical integral of $Q_1 - Q_2 - Q_R$ (Yanai et al. 1973), end up being physically realistic, namely, highly convective conditions (low SF) are associated with stronger vertical transport of moist static energy than stratiform conditions (high SF). At low levels, the atmosphere is drier for the high-SF cases (Fig. 9c), a reflection of the presence of unsaturated downdrafts in the squall-line trailing stratiform regions (Zipser 1977).

In Fig. 9e, positive PV anomalies (departures from the radar-period mean) are seen in the lower troposphere associated with convective cases (low SF) and in the midtroposphere associated with stratiform cases (high SF), consistent with the idea that positive PV anomalies are created where diabatic heating rates ($Q_1 - Q_R$) increase with height (e.g., Raymond and Jiang 1990). The midlevel PV anomaly associated the high-SF (stratiform) cases and its connection with top-heavy heating profile for this region have been previously documented (Hsieh and Cook 2008; Janiga and Thorncroft 2013; Tomassini et al. 2017), while the low-level PV anomaly associated with

low-SF (convective) cases has been recently reported in a modeling study by Russell and Aiyyer (2018). That the PV anomalies separately associated with convective and stratiform cases can be identified (Fig. 9e), but the heating distributions associated with each cannot (Fig. 9a) is likely explained by the fact that PV anomalies locally generated by latent heating processes are spread over larger areas as the convection moves through the region. Evidence for this effect will be shown in connection with composite squall line results in Section 3c. The PV anomaly patterns in Fig. 9e are consistent with those expected with leading-line/trailing stratiform squall-line systems (Hertenstein and Schubert 1991).

Nieto Ferreira et al. (2009) found that there were two predominant tracks of AEWs during the summer of 2006, a northerly track between 8° and 16°N and a southerly track between 2° and 6°N. Fifteen north-south oriented squall lines were observed in connection with the northerly AEW track approximately centered at the latitude of the track and 13 were associated with the southerly AEW track but centered well north of it. Many of these events are associated with the precipitation maxima seen in Fig. 5. Nieto Ferreira et al. (2009) found that stratiform rain fraction was significantly greater for the northerly track cases than the southerly track cases (47% vs. 33%, respectively).

The latitude range of EBAN (9° to 17°N) aligns well with the northerly track squall lines and that of EBAS (6.5° to 13.5°N) is more closely aligned with the southerly track squall lines (Fig. 1). Considering this, mean profiles have been computed for EBAN for the 15 northerly track cases and for EBAS for the 13 southerly track cases using the six-hourly sounding analyses before and after the time of squall line passage. The resulting profiles of divergence and vertical motion are shown in Fig. 10a,b. They are consistent with the idea of greater stratiform rain with the northerly track squall lines, namely, there is greater midlevel convergence and low-level sinking over EBAN than EBAS. The profiles of $Q_1 - Q_R$ and Q_2 (Fig. 10c,d) show greater low-level cooling and

evaporation over EBAN than EBAS, also consistent with greater stratiform rain to the north (also shown by Poan et al. (2014)). The latter finding is consistent with the study of Schumacher and Houze (2006) based on an analysis of 1998-2003 TRMM precipitation radar (PR) data.

While the results imply a greater stratiform rain fraction to the north, the vertical eddy flux of moist static energy F is greater over EBAN than EBAS (Fig. 10e), a seeming contradiction. One must conclude that there is more vigorous convection in the leading convective lines in the northerly track systems. This conclusion is supported by studies showing convection over the Sahel to be more vigorous and with higher echo tops than those farther south (e.g., Geerts and Dejene 2005; Zipser et al. 2006; Guy and Rutledge 2012). The higher levels of peak divergence and vertical motion over EBAN than EBAS (Fig. 10a,b) are consistent with this result.

c. Composite squall line results

A composite of 12 strongest and most extensive squall line events passing the MIT radar has been created by assigning time 0 for each as the time when the center of the leading convective line passed the radar site. Time series of surface variables associated with the composite squall line passage are shown in Fig. 11. The rainfall time series shows peak rainfall near time 0 followed by a secondary rainfall maximum 1.5-2 h later associated with the trailing stratiform precipitation system, which for the average squall line speed of 17.2 m s^{-1} corresponds to a distance of $\sim$90-120 km. Associated with the composite squall passages are a pressure rise of $\sim$3 hPa, temperature drop of $\sim$6°C, RH increase of $\sim$30%, and temporary shift of the wind from southwesterly to easterly followed by a return to southwesterly.

Shown in Fig. 12 are time series of temperature and specific humidity anomalies (departures from the 10 July-15 September monsoon period means) and relative humidity centered on the time

of passage of the composite leading convective line.[2] These results are from the gridded analyses averaged over the radar domain. Owing to the coarseness of the sounding network, details of the narrow convective lines cannot be resolved; nevertheless, broad-scale features of typical squall line systems are revealed in the composite. The temperature field (Fig. 12a) is characterized by a surface-based warm anomaly 10-18 h prior to line passage, followed by a surface cool anomaly peaking a few hours after squall line passage. These features are in part related to the diurnal cycle, namely, the majority of squall passages occurred during the morning hours. To illustrate this diurnal preference, red dots denoting the noon hour prior to squall passage are placed along the lower axis of Fig. 12a. The peak low-level warm anomaly is centered a few hours after the centroid of the red dots. In an analysis of the fields in Fig. 12 with the diurnal cycle filtered out (not shown) it is determined that approximately half the amplitude of the low-level anomalies of T, as well as those of q (Fig. 12b), are attributable to the diurnal cycle of surface latent and sensible heat fluxes. The remainder is associated with the squall line passage. Both q anomalies and relative humidity (Fig. 12b,c) show that moist conditions at low levels are observed just prior to convective line passage, immediately followed by moistening at midlevels and aloft. At upper levels moistening is observed both leading and trailing the convective line associated with spreading anvils aloft (Cetrone and Houze 2011). Warm and dry anomalies centered near 850 hPa existed 6 to 15 h following squall line passage associated with unsaturated downdrafts below the trailing stratiform precipitation systems (Zipser 1977).

Nieto Ferreira et al. (2009) showed that northerly track squall line cases occurred on the southern or cyclonic side of the 700-hPa AEJ axis at a time when the jet axis was centered near 15°N to the north of Niamey. In contrast, the southerly track cases occurred on the northern or anticy-

[2]Results in Fig. 12 are for all 12 squall lines. Separate composites for just the northerly track cases (7 events; results to be shown later) and southerly track cases (5 events) using the designations of Nieto Ferreira et al. (2009) yield similar results for these particular fields.

clonic side of the AEJ axis when it was centered south of Niamey's 13.5°N latitude. Given that the northerly track systems evolved in a background environment of cyclonic vorticity, we focus on the 7 out of the 12 events that were on the northerly track, which occurred between July 19 and August 28 (these cases are indicated in Table 1). Figure 13 shows divergence, absolute vorticity, and potential vorticity for the northerly track events. Once again, detailed features associated with the convective line cannot be resolved; however, prominent mesoscale characteristic features of LL/TS squall lines can be observed. First, there is an extended period of (1) low-level convergence prior to storm passage and low-level divergence following passage and (2) a deep layer of convergence maximizing near the melting level and divergence aloft (near 200 hPa) in the trailing stratiform region (Fig. 13a), reported elsewhere in African squall lines and MCSs in the tropics and midlatitudes (e.g., Houze 1977; Zipser 1977; Maddox 1983; Chong et al. 1987; Mapes and Houze 1995; Kingsmill and Houze 1999). Second, accompanying the convergence is an increase in the magnitude and a vertical spreading of the absolute vorticity maximum following convective line passage (Fig. 13b). Prior to the convective line passage, there is a deep layer (700-350 hPa) of high values of background absolute vorticity, which can also be seen in a north-south cross section averaged between 2 and 3°E at t = 0 h encompassing Niamey's longitude (Fig. 14a). Comparing Fig. 14a to Fig. 7b, it can be seen that the axis of the AEJ and mid-troposphere absolute vorticity maximum is shifted northward by about 2.5° latitude for the 7 northerly track cases compared to the monsoon-period mean.

Corresponding to the increase in absolute vorticity, there is an amplification of PV to the rear of the convective line (lower panel, Fig. 13c). However, the principal axis of peak values of PV is 1-2 km above that of absolute vorticity. The explanation for this difference lies in the fact that southward extension of the tongue of high PV associated with the Saharan heat low has an axis that resides between 400 and 500 hPa (Fig. 14b), which is evident in the pre-squall environment (Fig.

13c). Figure 14b is a clear indication of the equatorward dynamical extension along isentropes of the stable layer of the Sahara, as proposed by Schubert et al. (1995). This PV maximum is distinct from the lower-level PV maximum associated with the AEJ (Fig. 14). The upper-level PV maximum is amplified during the passage of the squall line as a result of advection of higher PV from the north during the passage of the AEW (not shown). The strongest convergence is at the melting layer (Fig. 13a), as observed elsewhere in tropical MCSs (e.g., Mapes and Houze 1995; Mapes and Zuidema 1996), such that the background absolute vorticity is most amplified at this level (Fig. 13b). The net effect is to cause the trailing PV maximum to strengthen and expand vertically, bulging downward toward the 0°C level.

Figure 15 shows vertical motion, apparent heat source Q_1, and apparent moisture sink Q_2 for the composite northerly track squall line. Rising motion is observed at low levels ahead of the convective line followed by a broad area of ascent aloft and sinking at low levels in the trailing stratiform precipitation region (Fig. 14a). Considering that the production of potential vorticity PV is approximated by $dPV/dt \simeq -g(\zeta_p + f)\partial\dot{\theta}/\partial p$, where $\dot{\theta} = \frac{\theta}{T}Q_1$, the strong vertical gradient in Q_1 near the melting level accounts for the large values of PV that develop there (e.g., Raymond and Jiang 1990; Hertenstein and Schubert 1991). The structure of Q_2 to the rear of the convective line is also characteristic of stratiform precipitation, namely, drying aloft and evaporative moistening at low levels; however, the peak in Q_2 is not as horizontally extensive as it is for Q_1. As in the case of Fig. 12, the high-amplitude, near-surface maxima of Q_1 and Q_2 are largely influenced by boundary layer turbulent exchanges.

To better elucidate the impacts of the northerly track squall lines on the PV distribution, anomaly fields (with respect to the monsoon-period means) of vorticity, stability, and PV are shown in Fig. 16. A vorticity maximum in the trailing stratiform precipitation region is centered between 600 and 700 hPa (Fig. 16a), slightly below the peak in total absolute vorticity at the melting level (Fig.

13b). This result indicates that the anomalous cyclonic circulation generated by the squall system at Niamey's latitude resides near the level of the axis of the AEJ (Fig. 14a). An analysis of the 700-hPa circulation associated with the passage of northerly track squall lines by Nieto Ferreira et al. (2009) shows a strong cyclonic vortex at that level to the rear of the storms as they pass the longitude of Niamey. Another prominent feature in the stratiform region, however, is enhanced stabilization at the melting layer (Fig. 16b), as commonly observed in tropical MCSs (Johnson et al. 1996). This feature is connected with the melting of hydrometeors and is associated with the upward shift in the PV anomaly maximum from the level of the vorticity maximum (Fig. 16a) to near 575 hPa (Figs. 16b,c). This position of the PV anomaly maximum corresponds well to the location of the strong vertical gradient in Q_1 seen in Fig. 15b. Using from this figure an estimate of the vertical gradient of Q_1 of 6 K 100 hPa^{-1} yields of PV production rate of 0.10 PVU 12 h^{-1}. This value is in good agreement with the PV anomaly increase observed following squall line passage (Fig. 16c). The fact that the isothermal layer associated with melting is only several hundred meters deep (Findeisen 1940) creates a challenge for the proper representation of this PV anomaly in numerical simulations and reanalyses.

Finally, the impact of the northerly track squall lines on the PV field as they passed the Niamey radar site is illustrated in Fig. 17. PV and streamline anomalies for the period 24 hours before to 24 hours after convective line passage at Niamey at 700 and 600 hPa are shown, along with estimates of the dimensions and orientation of the convective line (green segments). The plots at 600 hPa are close to the average 0°C level at 575 hPa. At 700 hPa, the convective line is located to the north and slightly leads the circulation center as it passes south of the radar site, as shown in Nieto Ferreira et al. (2009). However, at 600 hPa, the evolution of the PV field is remarkably different, with a pronounced growth and expansion of a positive PV anomaly to the rear of the convective line following passage. The strong vertical gradient in Q_1 near the melting level (Fig.

15) has left a prominent positive PV anomaly at this level in the squall line stratiform region and its wake.

To summarize, a PV maximum associated with the Saharan heat low resides between 400 and 500 hPa in the pre-squall environment, which becomes amplified and vertically extended during squall line passage (Fig. 13c). However, a new PV anomaly appears centered near the melting level in the squall line trailing stratiform region caused by the strong vertical gradient in latent heating there (Fig. 16c). *These results provide evidence of a coupling and merging of two PV sources following the passage of West African squall lines – one associated with the deep convective boundary layer over the Saharan desert and another with strong vertical gradients in diabatic heating near the melting level in the stratiform region – that ends up creating a prominent mid-tropospheric positive PV maximum to the rear of the squall line systems.*

These findings provide an observational context to previous studies of PV generation by convection in AEWs based on reanalyses and model results. Numerical simulations (Berry and Thorncroft 2012) and reanalysis products (Janiga and Thorncroft 2013), which depend in part on convective parameterizations, indicate maximum PV generation near 700 hPa or the level of the AEJ. However, the composite results from these AMMA analyses indicate that the PV anomaly arising from squall line passage resides closer to the melting level ($\sim$575 hPa) as a result of the strong vertical gradient of latent heating in the stratiform region there. This convective influence, when combined with the PV maximum extending southward from the Saharan heat low, results in a relatively deep, mid-tropospheric PV maximum peaking in the 400-600 hPa layer to the rear of squall lines.

The potential role of the midlevel positive PV anomaly atop the Saharan boundary layer in AEW dynamics has recently been explored in a modeling study by Tomassini (2018). Using the Met Office Unified Model Global Atmosphere at 5-km grid spacing, he found that one mechanism

by which PV is enhanced in AEW disturbances is through a nocturnal descent of the Saharan-based mid-troposphere PV maximum to lower levels (1.0-2.4 km), which then allows the positive PV signature to be incorporated into and amplify the AEW circulation. Preliminary analyses of the diurnal cycle of the positive PV anomaly originating over the Sahara based on the AMMA sounding networks do not indicate such a diurnal fluctuation in its altitude (not shown); however, further analysis of the diurnal cycle of the convective systems and their environment is currently underway.

4. Summary and conclusions

Atmospheric soundings and radar observations from the 2006 AMMA field campaign have been used to diagnose the impact of West African squall lines on the regional environments following their passage. Sounding data that comprised two quadrilaterals established over central West Africa during AMMA (Parker et al. 2008) form the principal results of this study. Additionally, gridded analyses over all of West Africa were produced using soundings from numerous land sites, ships, aircraft dropsondes, driftsondes, pibals, and wind profilers to provide a larger-scale context to the core analysis region. The radar observations utilized were from the MIT radar deployed at Niamey, Niger, for the period 5 July to 27 September. During this period, 28 squall lines were observed to pass Niamey, the majority of which were associated with the passage of African Easterly Waves or AEWs (Nieto Ferreira et al. 2009; Rickenbach et al. 2009; Guy et al. 2011). A subset of the strongest squall lines was selected for a composite analysis of the systems.

To provide a large-scale context, meteorological conditions over West Africa before and during the period of radar operations are documented. These periods are referred to as “pre-monsoon” and “monsoon” periods, respectively. Monsoon rainfall over the Sahel began around the time of the initiation of radar operations, marked by the beginning of westward-propagating squall lines

that accounted for 82% of the total rainfall during the radar period (Nieto Ferreira et al. 2009). As the monsoon period began, the axis of the African Easterly Jet (AEJ) shifted northward by about 5°, accompanied by a strengthening of the reversal in the north-south gradient of potential vorticity (PV). However, throughout the entire period, a prominent tongue of high-PV peaking in the 400-500 hPa layer extended southward from the Sahara. This PV maximum is a consequence of turbulent mixing atop deep convective boundary layers over the hot Saharan desert Karyampudi and Carlson (1988); Cuesta et al. (2009); Messager et al. (2010); Garcia-Carreras et al. (2015) strengthened by shortwave radiative heating of the dust that is lofted from the surface to the top of the mixed layer or Saharan Air Layer (Carlson and Prospero (1972); Karyampudi and Carlson (1988).

Using a partitioning of the radar observations of precipitation into convective and stratiform components (Rickenbach et al. 2009; Guy et al. 2011), it is shown that convective heating in the West African precipitation systems serves to generate positive PV anomalies at low levels and negative anomalies aloft, whereas heating in the stratiform regions is effective in generating a large positive PV anomaly in the mid-troposphere (e.g., Hertenstein and Schubert 1991).

In their analysis of squall lines passing Niamey, Nieto Ferreira et al. (2009) found some were associated with northerly track AEWs and some with southerly track AEWs. The northerly track cases occurred on the southern or cyclonic side of the AEJ. Selecting a subset of the seven strongest of the northerly track cases, it is found that the latent heating in the trailing stratiform region of the squall lines (heating aloft and cooling below the 0°C level) leads to strong convergence in the mid-troposphere peaking near the melting level, a peak vorticity anomaly between 600 and 700 hPa, and a PV anomaly maximum near the melting level. The location of the PV anomaly maximum near the 0°C level is due to the strong vertical gradient in latent heating associated with the melting of hydrometeors. When combined with the positive PV anomaly between 400

and 500 hPa extending southward from the Saharan heat low, the two sources of PV result in a relatively deep (600-400 hPa) positive PV maximum trailing the squall lines. *These results point to an important coupling between disparate processes over West Africa in the mid-tropospheric PV structure of AEW-related squall lines, namely, boundary-layer heating over deserts and latent heating in the stratiform regions of such systems.*

Investigations into the PV dynamics of AEWs have been carried out in recent years using reanalyses and numerical simulations (Berry and Thorncroft 2012; Janiga and Thorncroft 2013; Tomassini et al. 2017; Tomassini 2018). This study represents an extension of those works based directly on observations and therefore largely independent of model parameterizations. Further work is underway to explore the mechanisms involved in the above processes as well as the role of the diurnal cycle.

Acknowledgments. We are indebted to Adam Davis for his initial work that motivated this research effort. Rosana Nieto Ferreira and Nick Guy generously provided MIT radar data as well as valuable discussions. We also acknowledge helpful interactions with Wayne Schubert regarding many aspects of this work. The radiative fluxes were provided by Zhe Feng and produced by Sally McFarlane, and Mathieu Nuret produced the humidity corrections for many of the AMMA soundings sites. This research has been supported by the National Aeronautics and Space Administration under Grants NNX10AG81G and NNX13AF74G and the National Science Foundation under Grants AGS-1360237 and AGS-1853633.

APPENDIX

AMMA sounding data inventory, humidity corrections, and budget-TRMM comparisons

A visual inventory of the sounding observations from the AMMA core sites is shown in Fig. A1. Three radiosonde types were used in AMMA: Vaisala RS80, Vaisala RS92, and MODEM. Following the 2006 field campaign, comparisons of sounding total-column precipitable water (PW) with estimates from ground-based GPS retrievals (Bock et al. 2007) indicated significant humidity biases in both the Vaisala and MODEM sondes. For example, the Vaisala RS80 sondes at Niamey were shown to have a day-time dry bias of up to 14% at low-levels increasing to greater than 20% at upper-levels. Based on these findings, Nuret et al. (2008) designed and implemented a statistical correction procedure to reduce the RS80 dry bias to the accuracy level of the more reliable RS92 sonde. Further corrections, using a method similar to Vömel et al. (2007), were then applied to minimize the daytime dry bias found in the RS92 sondes and the modified-RS80 sondes. An additional correction following Miloshevich et al. (2009) was applied to all Vaisala soundings to reduce a small (few percent) night-time moist bias. The MODEM sondes at Ougadougou exhibited a modest nighttime moist bias (4-8% in the lower and mid troposphere) and daytime dry bias ($\sim$10% at lower-levels). These biases were reduced using a statistical method as in Nuret et al. (2008). Unfortunately, similar corrections attempted at the other sites using MODEM sondes (i.e., Cotonou and Parakou) resulted in no obvious bias reduction when compared with independent PW estimates, and thus the MODEM humidity profiles from these sites remain uncorrected.

In order to investigate the ability of the sounding networks in providing reliable results, a comparison between the moisture (Q_2) budget and TRMM rainfall over EBAN and EBAS has been

made (Fig. A2). Since measurements of surface fluxes are not available over the region, ECMWF reanalysis fluxes are utilized over the domains. While the mean values compare favorably, the correlations between the two estimates, 0.41 for EBAN and 0.64 for EBAS, are rather poor. This situation contrasts markedly with comparisons over the open ocean (e.g., Johnson and Ciesielski 2013) where there are (1) fewer complications in the budgets due to topography, (2) more reliable estimates of surface latent heat fluxes, and (3) TRMM 3B42 estimates are more reliable than over land (e.g., Ebert et al. 2007). In the AMMA domains, both stations Agadez and Abuja are near localized higher terrain features, the Aïr Mountains and Jos Plateau, respectively (Figs. 2 and 4). Such terrain features are known to contaminate budgets by locally disrupting the low-level flow, as in the case of the island of Sri Lanka impacting budgets for the northern sounding array in DYNAMO (Ciesielski et al. 2014). In addition, the EBAN is comprised of only three sites as compared to four for EBAS, which also has a site in its interior. Katsumata et al. (2011) demonstrated how a quadrilateral sounding array does a superior job of describing the structure of tropical waves than a triangular array. Consequently, complications in both budget and satellite estimates of rainfall degrade intercomparisons of the two products. Nevertheless, we utilize the sounding data from the AMMA networks since they represent the densest set of sounding observations ever obtained over West Africa.

References

Agustí-Panareda, A., and Coauthors, 2009: Radiosonde humidity bias correction over the West African region for the special AMMA reanalysis at ECMWF. *Quart. J. Roy. Meteor. Soc.*, **135 (640)**, 595–617, doi:10.1002/qj.396.

Agustí-Panareda, A., and Coauthors, 2010: The ECMWF re-analysis for the AMMA observational campaign. *Quart. J. Roy. Meteor. Soc.*, **136 (651)**, 1457–1472, doi:10.1002/qj.662.

Aspliden, C. I., Y. Tourre, and J. B. Sabine, 1976: Some climatological aspects of West African disturbance lines during GATE. *Mon. Wea. Rev.*, **104 (8)**, 1029–1035, doi:10.1175/1520-0493(1976)104⟨1029:SCAOWA⟩2.0.CO;2.

Berry, G. J., and C. Thorncroft, 2005: Case study of an intense African easterly wave. *Mon. Wea. Rev.*, **133 (4)**, 752–766, doi:10.1175/MWR2884.1.

Berry, G. J., and C. D. Thorncroft, 2012: African easterly wave dynamics in a mesoscale numerical model: The upscale role of convection. *J. Atmos. Sci.*, **69 (4)**, 1267–1283, doi:10.1175/JAS-D-11-099.1.

Bock, O., F. Guichard, S. Janicot, J. P. Lafore, M.-N. Bouin, and B. Sultan, 2007: Multiscale analysis of precipitable water vapor over Africa from GPS data and ECMWF analyses. *Geophys. Res. Lett.*, **34 (9)**, doi:10.1029/2006GL028039.

Burpee, R. W., 1972: The origin and structure of easterly waves in the lower troposphere of North Africa. *J. Atmos. Sci.*, **29 (1)**, 77–90, doi:10.1175/1520-0469(1972)029⟨0077:TOASOE⟩2.0.CO;2.

Burpee, R. W., 1974: Characteristics of North African easterly waves during the summers of 1968 and 1969. *J. Atmos. Sci.*, **31 (6)**, 1556–1570, doi:10.1175/1520-0469(1974)031⟨1556:CONAEW⟩2.0.CO;2.

Carlson, T. N., 1969: Synoptic histories of three African disturbances that developed into Atlantic hurricanes. *Mon. Wea. Rev.*, **97 (3)**, 256–276, doi:10.1175/1520-0493(1969)097⟨0256:SHOTAD⟩2.3.CO;2.

Carlson, T. N., and J. M. Prospero, 1972: The large-scale movement of Saharan air outbreaks over the northern equatorial Atlantic. *J. Appl. Meteor.*, **11 (2)**, 283–297, doi:10.1175/1520-0450(1972)011⟨0283:TLSMOS⟩2.0.CO;2.

Cetrone, J., and R. A. Houze, 2011: Leading and trailing anvil clouds of West African squall lines. *J. Atmos. Sci.*, **68 (5)**, 1114–1123, doi:10.1175/2011JAS3580.1.

Chalon, J. P., G. Jaubert, J. P. Lafore, and F. Roux, 1988: The West African squall line observed on 23 June 1981 during COPT 81: Mesoscale structure and transports. *J. Atmos. Sci.*, **45 (19)**, 2744–2763, doi:10.1175/1520-0469(1988)045⟨2744:TWASLO⟩2.0.CO;2.

Charney, J. G., and M. E. Stern, 1962: On the stability of internal baroclinic jets in a rotating atmosphere. *J. Atmos. Sci.*, **19 (2)**, 159–172, doi:10.1175/1520-0469(1962)019⟨0159:OTSOIB⟩2.0.CO;2.

Chong, M., P. Amayenc, G. Scialom, and J. Testud, 1987: A tropical squall line observed during the COPT 81 experiment in West Africa. Part 1: Kinematic structure inferred from dual-doppler radar data. *Mon. Wea. Rev.*, **115 (3)**, 670–694, doi:10.1175/1520-0493(1987)115⟨0670:ATSLOD⟩2.0.CO;2.

Ciesielski, P. E., R. H. Johnson, K. Yoneyama, and R. K. Taft, 2014: Mitigation of Sri Lanka island effects in Colombo sounding data and its impact on DYNAMO analyses. *J. Meteor. Soc. Japan*, **92 (4)**, 385–405, doi:10.2151/jmsj.2014-407.

Cohn, S. A., and Coauthors, 2013: Driftsondes: Providing in situ long-duration dropsonde observations over remote regions. *Bull. Amer. Meteor. Soc.*, **94 (11)**, 1661–1674, doi:10.1175/BAMS-D-12-00075.1.

Cuesta, J., J. H. Marsham, D. J. Parker, and C. Flamant, 2009: Dynamical mechanisms controlling the vertical redistribution of dust and the thermodynamic structure of the West Saharan atmospheric boundary layer during summer. *Atmospheric Science Letters*, **10 (1)**, 34–42, doi: 10.1002/asl.207.

Dickinson, M., and J. Molinari, 2000: Climatology of sign reversals of the meridional potential vorticity gradient over Africa and Australia. *Mon. Wea. Rev.*, **128 (11)**, 3890–3900, doi:10.1175/1520-0493(2001)129⟨3890:COSROT⟩2.0.CO;2.

Diedhiou, A., S. Janicot, A. Viltard, and P. de Félice, 2002: Energetics of easterly wave disturbances over west africa and the tropical atlantic: a climatology from the 1979–95 ncep/ncar reanalyses. *Climate Dynamics*, **18 (6)**, 487–500, doi:10.1007/s00382-001-0195-7, URL https://doi.org/10.1007/s00382-001-0195-7.

Duvel, J. P., 1990: Convection over tropical Africa and the Atlantic ocean during northern summer. Part II: Modulation by easterly waves. *Mon. Wea. Rev.*, **118 (9)**, 1855–1868, doi: 10.1175/1520-0493(1990)118⟨1855:COTAAT⟩2.0.CO;2.

Ebert, E. E., J. E. Janowiak, and C. Kidd, 2007: Comparison of near-real-time precipitation estimates from satellite observations and numerical models. *Bull. Amer. Meteor. Soc.*, **88 (1)**, 47–64, doi:10.1175/BAMS-88-1-47.

Eliassen, A., 1983: The Charney-Stern theorem on barotropic-baroclinic instability. *Pure Appl. Geophys.*, **121 (3)**, 563–572, doi:10.1007/BF02590155.

Findeisen, W., 1940: The formation of the 0°C isothermal layer and fractocumulus under nimbostratus. *Meteorolog. Z.*, **57**, 49–54.

Fink, A. H., and A. Reiner, 2003: Spatiotemporal variability of the relation between African easterly waves and west African squall lines in 1998 and 1999. *J. Geophys. Res.*, **108 (D11)**, doi:10.1029/2002JD002816.

Fink, A. H., D. G. Vincent, and V. Ermert, 2006: Rainfall types in the West African Sudanian Zone during the summer monsoon 2002. *Mon. Wea. Rev.*, **134 (8)**, 2143–2164, doi:10.1175/MWR3182.1.

Garcia-Carreras, L., and Coauthors, 2015: The turbulent structure and diurnal growth of the Saharan atmospheric boundary layer. *J. Atmos. Sci.*, **72 (2)**, 693–713, doi:10.1175/JAS-D-13-0384.1.

Geerts, B., and T. Dejene, 2005: Regional and diurnal variability of the vertical structure of precipitation systems in Africa based on spaceborne radar data. *J. Climate*, **18 (7)**, 893–916, doi:10.1175/JCLI-3316.1.

Guy, N., and S. A. Rutledge, 2012: Regional comparison of West African convective characteristics: a TRMM-based climatology. *Quart. J. Roy. Meteor. Soc.*, **138 (666)**, 1179–1195, doi:10.1002/qj.1865.

Guy, N., S. A. Rutledge, and R. Cifelli, 2011: Radar characteristics of continental, coastal, and maritime convection observed during AMMA/NAMMA. *Quart. J. Roy. Meteor. Soc.*, **137 (658)**, 1241–1256, doi:10.1002/qj.839.

Hamilton, R. A., and J. W. Archbold, 1945: Meteorology of Nigeria and adjacent territory. *Quart. J. Roy. Meteor. Soc.*, **71 (309-310)**, 231–264, doi:10.1002/qj.49707130905.

Hartmann, D. L., H. H. Hendon, and R. A. Houze, Jr., 1984: Some implications of the mesoscale circulations in tropical cloud clusters for large-scale dynamics and climate. *J. Atmos. Sci.*, **41**, 113–121.

Hertenstein, R. F. A., and W. H. Schubert, 1991: Potential vorticity anomalies associated with squall lines. *Mon. Wea. Rev.*, **119 (7)**, 1663–1672, doi:10.1175/1520-0493(1991)119⟨1663:PVAAWS⟩2.0.CO;2.

Hodges, K. I., and C. D. Thorncroft, 1997: Distribution and statistics of African mesoscale convective weather systems based on the ISCCP Meteosat imagery. *Mon. Wea. Rev.*, **125 (11)**, 2821–2837, doi:10.1175/1520-0493(1997)125⟨2821:DASOAM⟩2.0.CO;2.

Houze, R. A., Jr., 1977: Structure and dynamics of a tropical squall-line system. *Mon. Wea. Rev.*, **105**, 1540–1567, doi:10.1175/1520-0493(1977)105⟨1540:SADOAT⟩2.0.CO;2.

Houze, R. A., Jr., 1982: Cloud clusters and large-scale vertical motion in the tropics. *J. Meteor. Soc. Japan*, **60**, 396–410.

Hsieh, J.-S., and K. H. Cook, 2007: A study of the energetics of African easterly waves using a regional climate model. *J. Atmos. Sci.*, **64 (2)**, 421–440, doi:10.1175/JAS3851.1.

Hsieh, J.-S., and K. H. Cook, 2008: On the instability of the African easterly jet and the generation of African waves: Reversals of the potential vorticity gradient. *J. Atmos. Sci.*, **65 (7)**, 2130–2151, doi:10.1175/2007JAS2552.1.

Huffman, G. J., R. F. Adler, D. T. Bolvin, G. Gu, E. J. Nelkin, K. P. Bowman, E. F. Stocker, and D. B. Wolff, 2007: The TRMM multi-satellite precipitation analysis: Quasi-global, multi-year, combined-sensor precipitation estimates at fine scale. *J. Hydrometeor.*, **8**, 33–55, doi:10.1175/JHM560.1.

Janicot, S., and Coauthors, 2008: Large-scale overview of the summer monsoon over west africa during the amma field experiment in 2006. *Annales Geophysicae*, **26 (9)**, 2569–2595, doi:10.5194/angeo-26-2569-2008, URL https://www.ann-geophys.net/26/2569/2008/.

Janiga, M. A., and C. D. Thorncroft, 2013: Regional differences in the kinematic and thermodynamic structure of African easterly waves. *Quart. J. Roy. Meteor. Soc.*, **139 (675)**, 1598–1614, doi:10.1002/qj.2047.

Janiga, M. A., and C. D. Thorncroft, 2014: Convection over Tropical Africa and the East Atlantic during the West African Monsoon: Regional and Diurnal Variability. *J. Climate*, **27**, 4159–4188, doi:10.1175/JCLI-D-13-00449.1.

Johnson, R. H., 1984: Partitioning tropical heat and moisture budgets into cumulus and mesoscale components: Implications for cumulus parameterization. *Mon. Wea. Rev.*, **112**, 1590–1601.

Johnson, R. H., and P. E. Ciesielski, 2013: Structure and properties of Madden-Julian Oscillations deduced from DYNAMO sounding arrays. *J. Atmos. Sci.*, **70**, 3157–3179, doi: 10.1175/JAS-D-13-065.1.

Johnson, R. H., P. E. Ciesielski, and K. A. Hart, 1996: Tropical inversions near the 0°C level. *J. Atmos. Sci.*, **53**, 1838–1855.

Jones, C., N. Mahowald, and C. Luo, 2004: Observational evidence of African desert dust intensification of easterly waves. *Geophys. Res. Lett.*, **31 (17)**, doi:10.1029/2004GL020107.

Karyampudi, V. M., and T. N. Carlson, 1988: Analysis and numerical simulations of the Saharan Air Layer and its effect on easterly wave disturbances. *J. Atmos. Sci.*, **45 (21)**, 3102–3136, doi:10.1175/1520-0469(1988)045⟨3102:AANSOT⟩2.0.CO;2.

Karyampudi, V. M., and H. F. Pierce, 2002: Synoptic-scale influence of the Saharan Air Layer on tropical cyclogenesis over the eastern Atlantic. *Mon. Wea. Rev.*, **130 (12)**, 3100–3128, doi: 10.1175/1520-0493(2002)130⟨3100:SSIOTS⟩2.0.CO;2.

Katsumata, M., P. E. Ciesielski, and R. H. Johnson, 2011: Evaluation of budget analysis during MISMO. *J. Appl. Meteor. Climatol.*, **40**, 241–254.

Kiladis, G. N., C. D. Thorncroft, and N. M. J. Hall, 2006: Three-dimensional structure and dynamics of African easterly waves. part I: Observations. *J. Atmos. Sci.*, **63 (9)**, 2212–2230, doi: 10.1175/JAS3741.1.

Kingsmill, D. E., and R. A. Houze, Jr., 1999: Kinematic characteristics of air flowing into and out of precipitating convection over the west Pacific warm pool: An airborne doppler radar survey. *Quart. J. Roy. Meteor. Soc.*, **125 (556)**, 1165–1207, doi:10.1002/qj.1999.49712555605.

Lafore, J.-P., and Coauthors, 2011: Progress in understanding of weather systems in West Africa. *Atmospheric Science Letters*, **12 (1)**, 7–12, doi:10.1002/asl.335.

Laing, A. G., R. Carbone, V. Levizzani, and J. Tuttle, 2008: The propagation and diurnal cycles of deep convection in northern tropical Africa. *Quart. J. Roy. Meteor. Soc.*, **134**, 93 – 109, doi: 10.1002/qj.194.

Leary, C. A., and R. A. Houze, 1979: Melting and evaporation of hydrometeors in precipitation from the anvil clouds of deep tropical convection. *J. Atmos. Sci.*, **36 (4)**, 669–679, doi:10.1175/1520-0469(1979)036⟨0669:MAEOHI⟩2.0.CO;2.

Lothon, M., F. Saïd, F. Lohou, and B. Campistron, 2008: Observation of the diurnal cycle in the low troposphere of West Africa. *Mon. Wea. Rev.*, **136 (9)**, 3477–3500, doi:10.1175/2008MWR2427.1.

Maddox, R. A., 1983: Large-scale meteorological conditions associated with midlatitude, mesoscale convective complexes. *Mon. Wea. Rev.*, **111 (7)**, 1475–1493, doi:10.1175/1520-0493(1983)111⟨1475:LSMCAW⟩2.0.CO;2.

Mapes, B. E., and R. A. Houze, Jr., 1995: Diabatic divergence profiles in western Pacific mesoscale convective systems. *J. Atmos. Sci.*, **52**, 1807–1828.

Mapes, B. E., and P. Zuidema, 1996: Radiative-dynamical consequences of dry tongues in the tropical troposphere. *J. Atmos. Sci.*, **53**, 620–638.

Messager, C., D. J. Parker, O. Reitebuch, A. Agusti-Panareda, C. M. Taylor, and J. Cuesta, 2010: Structure and dynamics of the Saharan atmospheric boundary layer during the West African monsoon onset: observations and analyses from the research flights of 14 and 17 July 2006. *Quart. J. Roy. Meteor. Soc.*, **136 (S1)**, 107–124, doi:10.1002/qj.469.

Miller, M. A., and A. Slingo, 2007: The ARM Mobile Facility and its first international deployment: Measuring radiative flux divergence in West Africa. *Bull. Amer. Meteor. Soc.*, **88 (8)**, 1229–1244, doi:10.1175/BAMS-88-8-1229.

Miloshevich, L. M., H. Vömel, D. N. Whiteman, and T. Leblanc, 2009: Accuracy assessment and correction of Vaisala RS92 radiosonde water vapor measurements. *J. Geophys. Res.*, **114 (D11)**, doi:10.1029/2008JD011565.

Mohr, K. I., 2004: Interannual, monthly, and regional variability in the wet season diurnal cycle of precipitation in sub-Saharan Africa. *J. Climate*, **17 (12)**, 2441–2453, doi:10.1175/1520-0442(2004)017⟨2441:IMARVI⟩2.0.CO;2.

Nieto Ferreira, R., T. Rickenbach, N. Guy, and E. Williams, 2009: Radar observations of convective system variability in relationship to African easterly waves during the 2006 AMMA Special Observing Period. *Mon. Wea. Rev.*, **137 (12)**, 4136–4150, doi:10.1175/2009MWR2740.1.

Norquist, D. C., E. E. Recker, and R. J. Reed, 1977: The energetics of African wave disturbances as observed during Phase III of GATE. *Mon. Wea. Rev.*, **105 (3)**, 334–342, doi: 10.1175/1520-0493(1977)105⟨0334:TEOAWD⟩2.0.CO;2.

Nuret, M., J.-P. Lafore, F. Guichard, J.-L. Redelsperger, O. Bock, A. Agusti-Panareda, and J.-B. N'Gamini, 2008: Correction of humidity bias for Vaisala RS80-A sondes during the AMMA 2006 observing period. *J. Atmos. Oceanic Technol.*, **25 (11)**, 2152–2158, doi:10.1175/2008JTECHA1103.1.

Nuss, W. A., and D. W. Titley, 1994: Use of multiquadric interpolation for meteorological objective analysis. *Mon. Wea. Rev.*, **122 (7)**, 1611–1631, doi:10.1175/1520-0493(1994)122⟨1611:UOMIFM⟩2.0.CO;2.

Parker, D. J., and Coauthors, 2008: The AMMA radiosonde program and its implications for the future of atmospheric monitoring over Africa. *Bull. Amer. Meteor. Soc.*, **89 (7)**, 1015–1028, doi:10.1175/2008BAMS2436.1.

Payne, S. W., and M. M. McGarry, 1977: The relationship of satellite inferred convective activity to easterly waves over West Africa and the adjacent ocean during Phase III of GATE. *Monthly Weather Review*, **105 (4)**, 413–420, doi:10.1175/1520-0493(1977)105⟨0413:TROSIC⟩2.0.CO;2.

Poan, D. E., J.-P. Lafore, R. Roehrig, and F. Couvreux, 2014: Internal processes within the African easterly wave system. *Quart. J. Roy. Meteor. Soc.*, **141 (689)**, 1121–1136, doi:10.1002/qj.2420.

Powell, S. W., R. A. Houze, A. Kumar, and S. A. McFarlane, 2012: Comparison of simulated and observed continental tropical anvil clouds and their radiative heating profiles. *J. Atmos. Sci.*, **69 (9)**, 2662–2681, doi:10.1175/JAS-D-11-0251.1.

Raymond, D. J., and H. Jiang, 1990: A theory for long-lived mesoscale convective systems. *J. Atmos. Sci.*, **47**, 3067–3077.

Redelsperger, J.-L., C. D. Thorncroft, A. Diedhiou, T. Lebel, D. J. Parker, and J. Polcher, 2006: African Monsoon Multidisciplinary Analysis: An international research project and field campaign. *Bull. Amer. Meteor. Soc.*, **87 (12)**, 1739–1746, doi:10.1175/BAMS-87-12-1739.

Reed, R. J., D. C. Norquist, and E. E. Recker, 1977: The structure and properties of African Wave disturbances as observed during Phase III of GATE. *Mon. Wea. Rev.*, **105 (3)**, 317–333, doi:10.1175/1520-0493(1977)105⟨0317:TSAPOA⟩2.0.CO;2.

Rickenbach, T., R. Nieto Ferreira, N. Guy, and E. Williams, 2009: Radar-observed squall line propagation and the diurnal cycle of convection in Niamey, Niger, during the 2006 African Monsoon and Multidisciplinary Analyses Intensive Observing Period. *J. Geophys. Res.*, **114 (D3)**, doi:10.1029/2008JD010871.

Roux, F., 1988: The West African squall line observed on 23 June 1981 during COPT 81: Kinematics and thermodynamics of the convective region. *J. Atmos. Sci.*, **45 (3)**, 406–426, doi: 10.1175/1520-0469(1988)045⟨0406:TWASLO⟩2.0.CO;2.

Roux, F., J. Testud, M. Payen, and B. Pinty, 1984: West African squall-line thermodynamic structure retrieved from dual-doppler radar observations. *J. Atmos. Sci.*, **41 (21)**, 3104–3121, doi: 10.1175/1520-0469(1984)041⟨3104:WASLTS⟩2.0.CO;2.

Rowell, D. P., and J. R. Milford, 1993: On the generation of African squall lines. *J. Climate*, **6 (6)**, 1181–1193, doi:10.1175/1520-0442(1993)006⟨1181:OTGOAS⟩2.0.CO;2.

Russell, J. O. H., and A. R. Aiyyer, 2018: African easterly waves and convection: A potential vorticity perspective. *33rd Conference on Hurricanes and Tropical Meteorology*, Ponte Vedra, FL, Amer. Meteor. Soc.

Schubert, W. H., P. E. Ciesielski, C. Lu, and R. H. Johnson, 1995: Dynamical adjustment of the trade wind inversion layer. *J. Atmos. Sci.*, **52 (16)**, 2941–2952, doi:10.1175/1520-0469(1995)052⟨2941:DAOTTW⟩2.0.CO;2.

Schubert, W. H., P. E. Ciesielski, D. E. Stevens, and H.-C. Kuo, 1991: Potential vorticity modeling of the ITCZ and the Hadley Circulation. *J. Atmos. Sci.*, **48**, 1493–1509.

Schubert, W. H., S. R. Fulton, and R. F. A. Herttenstein, 1989: Balanced atmospheric response to squall lines. *J. Atmos. Sci.*, **46 (15)**, 2478–2483, doi:10.1175/1520-0469(1989)046⟨2478:BARTSL⟩2.0.CO;2.

Schumacher, C., and R. A. Houze, Jr., 2006: Stratiform precipitation production over sub-Saharan Africa and the tropical East Atlantic as observed by TRMM. *Quart. J. Roy. Meteor. Soc.*, **132 (620)**, 2235–2255, doi:10.1256/qj.05.121.

Schumacher, C., R. A. Houze, Jr., and I. Kraucunas, 2004: The tropical dynamical response to latent heating estimates derived from the trmm precipitation radar. *J. Atmos. Sci.*, **61**, 1341–1358.

Stull, R. B., 1988: *An Introduction to Boundary Layer Meteorology*. Kluwer Academic, 666 pp., doi:10.1007/978-94-009-3027-8.

Sultan, B., and S. Janicot, 2003: The West African monsoon dynamics. Part II: The "preonset" and "onset" of the summer monsoon. *J. Climate*, **16 (21)**, 3407–3427, doi:10.1175/1520-0442(2003)016⟨3407:TWAMDP⟩2.0.CO;2.

Thorncroft, C., and K. Hodges, 2001: African easterly wave variability and its relationship to Atlantic tropical cyclone activity. *J. Climate*, **14 (6)**, 1166–1179, doi:10.1175/1520-0442(2001)014⟨1166:AEWVAI⟩2.0.CO;2.

Thorncroft, C. D., and M. Blackburn, 1999: Maintenance of the African easterly jet. *Quart. J. Roy. Meteor. Soc.*, **125 (555)**, 763–786, doi:10.1002/qj.49712555502.

Tomassini, L., 2018: Mesoscale circulations and organized convection in African easterly waves. *J. Atmos. Sci.*, **75 (12)**, 4357–4381, doi:10.1175/JAS-D-18-0183.1.

Tomassini, L., D. J. Parker, A. Stirling, C. Bain, C. Senior, and S. Milton, 2017: The interaction between moist diabatic processes and the atmospheric circulation in African easterly wave propagation. *Quart. J. Roy. Meteor. Soc.*, **143 (709)**, 3207–3227, doi:10.1002/qj.3173.

Vömel, H., and Coauthors, 2007: Radiation dry bias of the Vaisala RS92 humidity sensor. *J. Atmos. Oceanic Technol.*, **24 (6)**, 953–963, doi:10.1175/JTECH2019.1.

Webster, P. J., and G. L. Stephens, 1980: Tropical upper-tropospheric extended clouds: Inferences from winter MONEX. *J. Atmos. Sci.*, **37 (7)**, 1521–1541, doi:10.1175/1520-0469(1980)037⟨1521:TUTECI⟩2.0.CO;2.

Wielicki, B. A., B. R. Barkstrom, E. F. Harrison, R. B. Lee, G. L. Smith, and J. E. Cooper, 1996: Clouds and the Earth's Radiant Energy System (CERES): An earth observing system experiment. *Bull. Amer. Meteor. Soc.*, **77 (5)**, 853–868, doi:10.1175/1520-0477(1996)077⟨0853:CATERE⟩2.0.CO;2.

Yanai, M., S. Esbensen, and J.-H. Chu, 1973: Determination of bulk properties of tropical cloud clusters from large-scale heat and moisture budgets. *J. Atmos. Sci.*, **30**, 611–627.

Zipser, E. J., 1977: Mesoscale and convective-scale downdrafts as distinct components of squall-line circulation. *Mon. Wea. Rev.*, **105**, 1568–1589, doi:10.1175/1520-0493(1977)105⟨1568:MACDAD⟩2.0.CO;2.

Zipser, E. J., D. J. Cecil, C. Liu, S. W. Nesbitt, and D. P. Yorty, 2006: Where are the most intense thunderstorms on earth? *Bull. Amer. Meteor. Soc.*, **87 (8)**, 1057–1072, doi:10.1175/BAMS-87-8-1057.

LIST OF TABLES

TABLE 1. Timing and properties of twelve squall line cases used in MCS composite. Time indicates center of convective line passage at the MIT radar site at Niamey. African Easterly Wave (AEW) track designation and squall line speed are from Nieto Ferreira et al. (2009). All squall lines were westward moving and, to a greater or lesser degree, had a leading-line/trailing stratiform structure. These cases were a subset of the 28 MCSs studied by Nieto Ferreira et al. (2009), Rickenbach et al. (2009), and Guy et al. (2011).

Month	Day	Time (UTC)[a]	AEW track	Convective line orientation	Squall line speed (m s^{-1})
July	14	0520	Southern	N-S	25
	17	0650	Southern	NNE-SSW	21
	19	0545	Northern	NNE-SSW	15
	22	0940	Northern	N-S	17
August	3	1410	Southern	N-S	15
	6	0800	Northern	NW-SE	10
	11	0340	Northern	N-S	16
	18	0840	Northern	NNE-SSW	16
	22	0325	Northern	NW-SE	14
	28	0240	Northern	N-S	17
September	12	1510	Southern	NW-SW	19
	24	0330	Southern	N-S	21

[a]Niamey local time = UTC + 1 hour

LIST OF FIGURES

Fig. 9. Vertical profiles of (a) radiative heating rate Q_R (thin curves) and convective heat source $Q_1 - Q_R$ (thick curves) in units of K day^{-1}, (b) apparent moisture sink Q_2 (K day^{-1}), (c) relative humidity (%, with respect to ice for sub-freezing temperatures), (d) vertical eddy flux of moist static energy F (W m^{-2}), and (e) potential vorticity anomaly (PVU = 10^{-6} K m^2 kg^{-1} s^{-1}) for MIT-radar-based average stratiform fraction SF of 82% (red) and 30% (black). In other words, the red (black) curves can be considered representative of precipitation events predominantly stratiform (convective) in nature. Curves show profiles when radar times matched up with sonde times during the period when radar data were available. . . 54

Fig. 10. Vertical profiles of (a) divergence (10^{-6} s^{-1}), (b) vertical motion (hPa h^{-1}), (c) convective heat source ($Q_1 - Q_R$; K day^{-1}), (d) apparent moisture sink Q_2 (K day^{-1}), and (e) vertical eddy flux of moist static energy F (W m^2) for squall line (MCS) passage at MIT radar site at Niamey for northerly track systems (EBAN) and southerly track systems (EBAS). Number of six-hourly sounding times used in the averages given in parentheses. 55

Fig. 11. (top to bottom) Time series relative to composite convective line passage of surface precipitation (mm h^{-1}), pressure (hPa), wind vectors (one full barb = 10 m s^{-1}), temperature (C), and relative humidity RH (%) at the Niamey ARM site. 56

Fig. 12. Time series relative to composite convective line passage of (a) temperature anomaly (°C) and (b) specific humidity anomaly (g kg^{-1}) representing departures from monsoon period (10 July–15 September) respective means, and (c) relative humidity RH (%, with respect to ice for $T < 0$°C) at Niamey radar site. Horizontal dashed lines denote 0°C level. Red dots at base of top panel indicate the time of noon prior to squall passage for the 12 cases. . . . 57

Fig. 13. Time series relative to composite convective line passage of (a) divergence (10^{-5} s^{-1}), (b) relative vorticity (10^{-5} s^{-1}), and (c) potential vorticity (PVU = 10^{-6} K m^2 kg^{-1} s^{-1}) at Niamey radar site. Horizontal dashed lines denote 0°C level. 58

Fig. 14. North-south cross sections (equator to 20°N) averaged from 2 to 3°E of (a) zonal wind (m s^{-1}, contours) and absolute vorticity (10^{-5} s^{-1}, shading) and (b) potential temperature (K, gray contours) and potential vorticity PV (PVU = 10^{-6} K m^2 kg^{-1} s^{-1}, contoured color field) for the 7 northerly track squall line cases. Stippling indicates where the north-south gradient of PV is negative. TRMM rainfall for the same cases is shown at bottom. Heavy solid lines are estimates of cloud-base height based on surface observations. Light blue line denotes the 0°C level. 59

Fig. 15. Time series relative to composite convective line passage of (a) vertical motion (hPa h^{-1}), (b) apparent heat source Q_1 (K day^{-1}), and (c) apparent moisture sink Q_2 (K day^{-1}) at Niamey radar site. Horizontal dashed lines denote 0°C level. 60

Fig. 16. Time series relative to composite convective line passage of anomalies of (a) vorticity (10^{-5} s^{-1}), (b) stability (K hPa^{-1}), and (c) potential vorticity (PVU = 10^{-6} K m^2 kg^{-1} s^{-1}) at Niamey radar site. Anomalies are relative to the monsoon period (10 July-15 September) mean fields. Horizontal dashed lines denote 0°C level. 61

Fig. 17. Succession of composite anomaly maps of PV and streamline fields at 700 and 600 hPa from 24 hours before to 24 hours after convective line passage at MIT radar site at Niamey (marked by stars in top panels). PV units are 10^{-6} K m^2 kg^{-1} s^{-1}. The streamline and PV anomalies are relative to the monsoon period (10 July-15 September) mean fields. Green line segments denote estimated positions, orientation, and dimension of convective line based on 15 m s^{-1} west-northwestward movement, information provided in Nieto Fer-

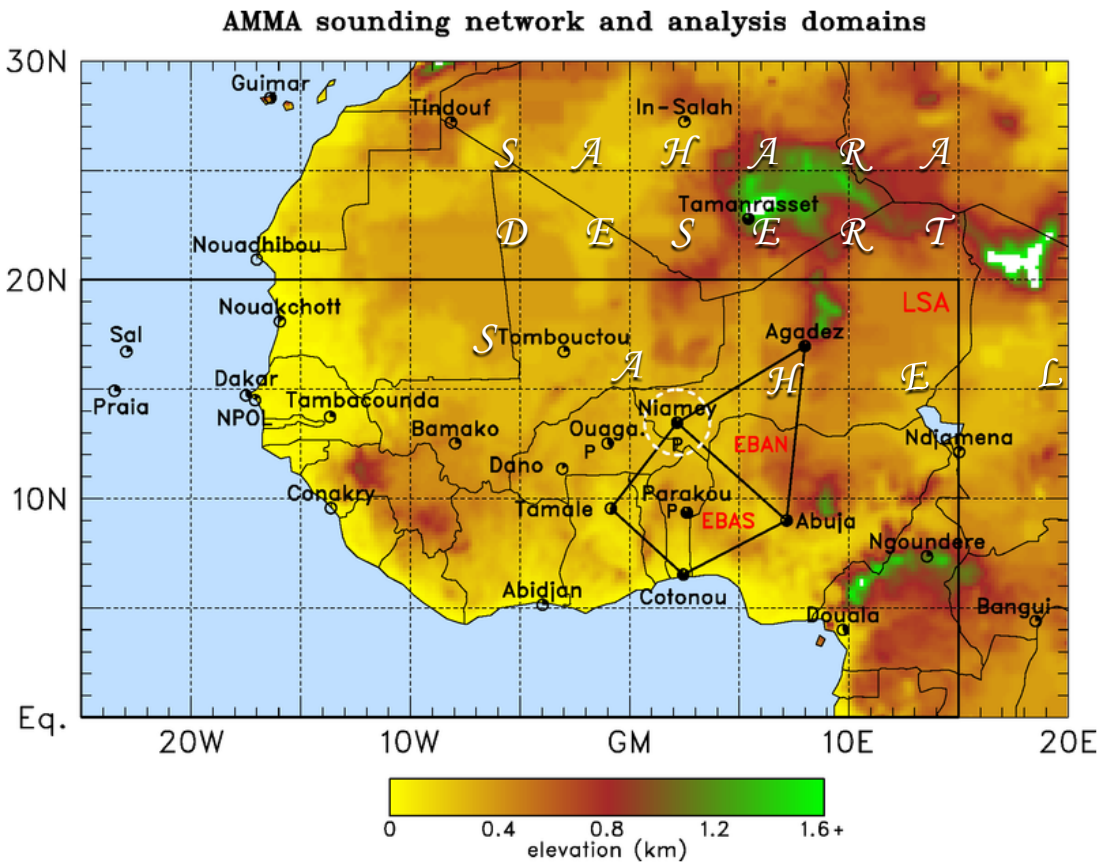

FIG. 1. AMMA sounding network for the period June-September 2006. Filling of the circles indicates the percent of soundings taken during this period assuming 4/day observations. Smaller polygons denote the enhanced budget arrays (EBAN, EBAS) with larger polygon (LSA) indicating the domain over which the gridded analysis was performed. 'P' symbols show the locations of profiler sites. Color shading over land indicates surface elevation with scale at bottom. Dashed circle at Niamey denotes 150-km range of MIT radar.

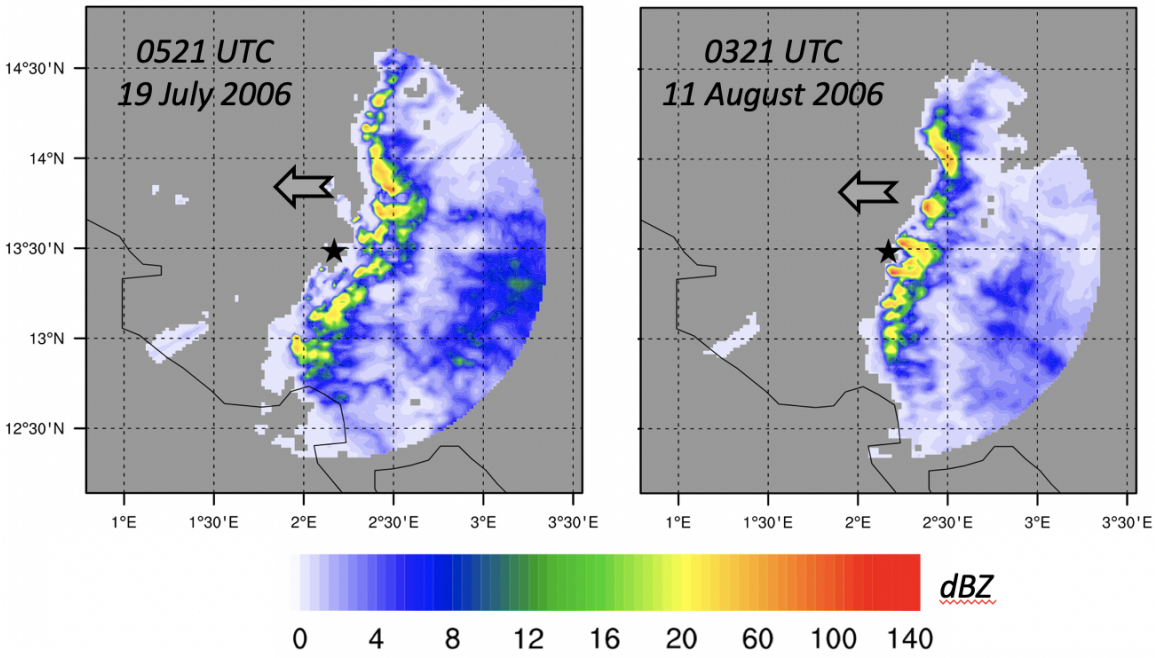

FIG. 2. Radar reflectivity images for two squall line cases on 19 July and 11 August 2006 as their convective lines were just about to pass the MIT radar site (indicated by star). The two squall lines were moving westward (indicated by arrows) at 15 and 16 m s^{-1}, respectively.

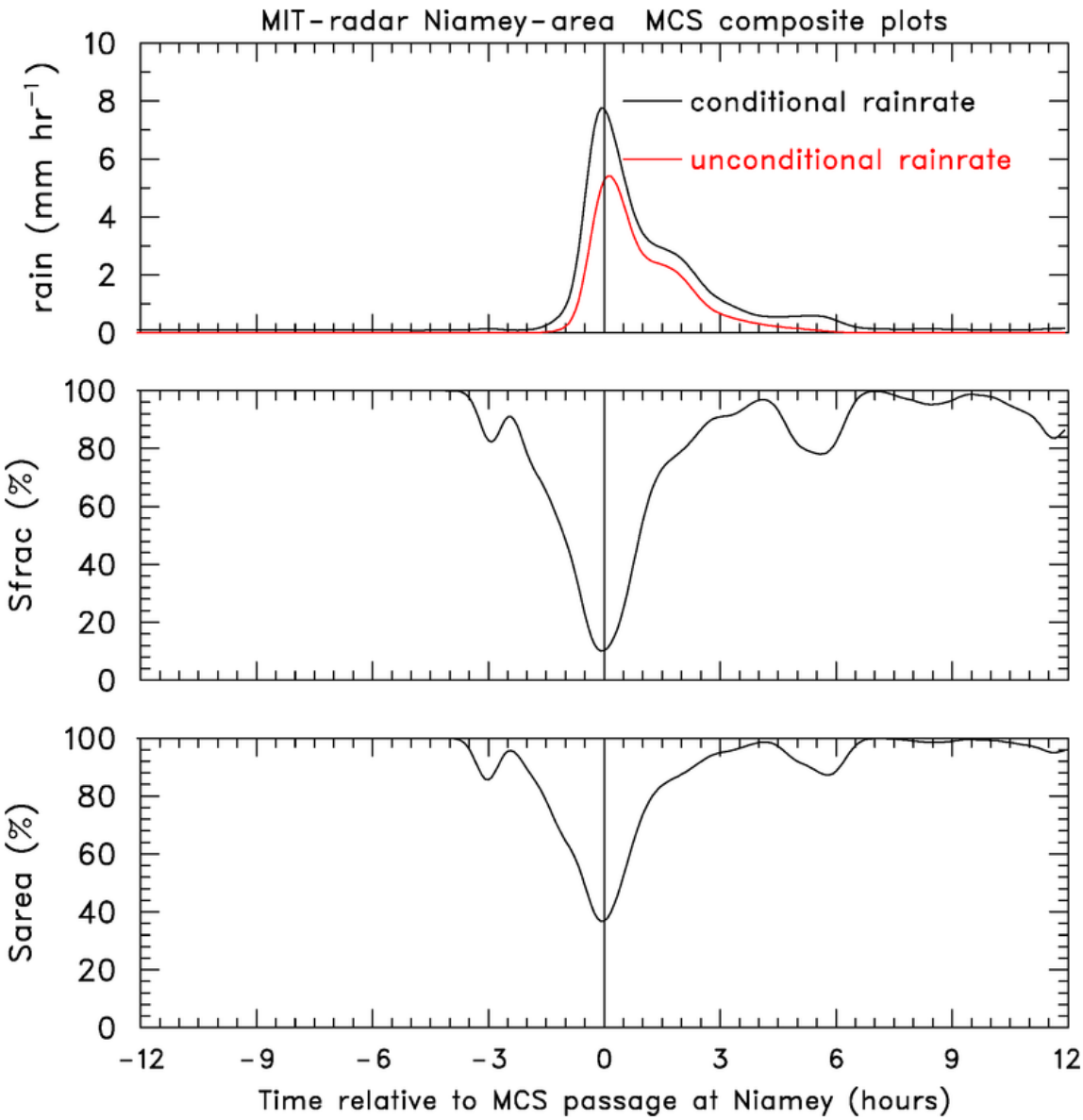

FIG. 3. Time series of radar-determined properties over a 20 km $\times$ 20 km area centered on Niamey of 12 composited squall lines. Time is relative to center of convective line passage at radar site. (top) Conditional and unconditional rain rates (mm h^{-1}) over specified area, (middle) stratiform rain fraction (%), and (bottom) stratiform rain area.

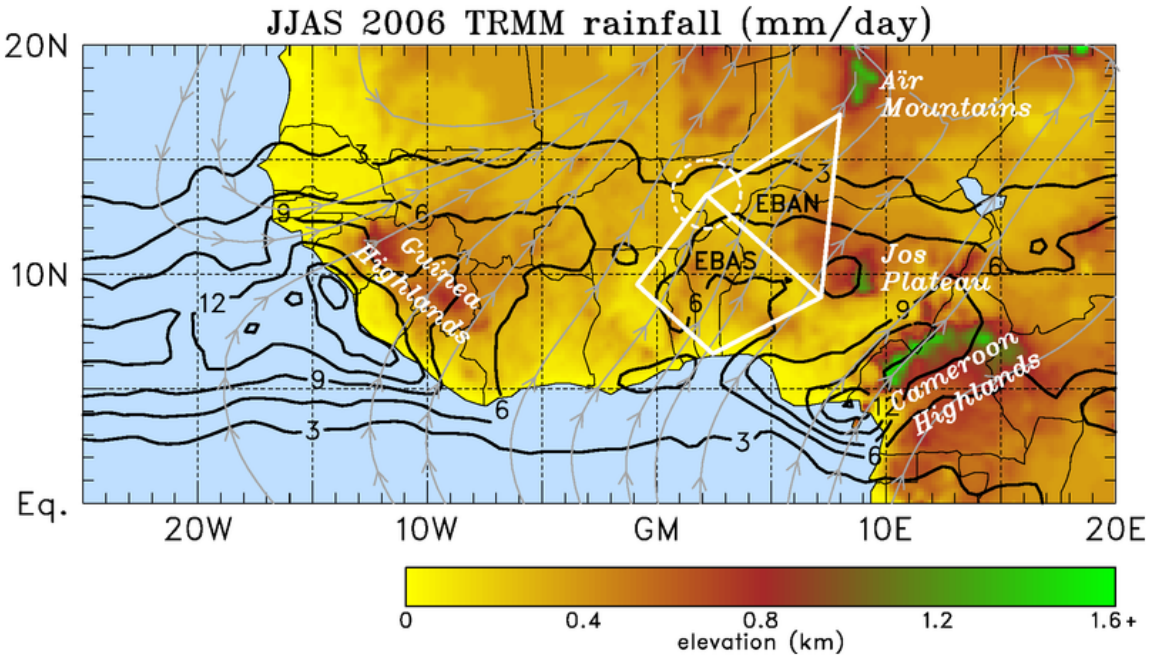

FIG. 4. June-September 2006 TRMM 3B42 rainfall (mm day^{-1}) and surface streamlines over Large Scale Array (LSA) domain of gridded sounding data. Relative to the surface flow, rainfall maxima occurred upstream of elevated terrain – the Guinea Highlands, Jos Plateau, and the Cameroon Highlands. Polygons indicate AMMA sounding networks, dashed circle the range of the MIT radar at Niamey.

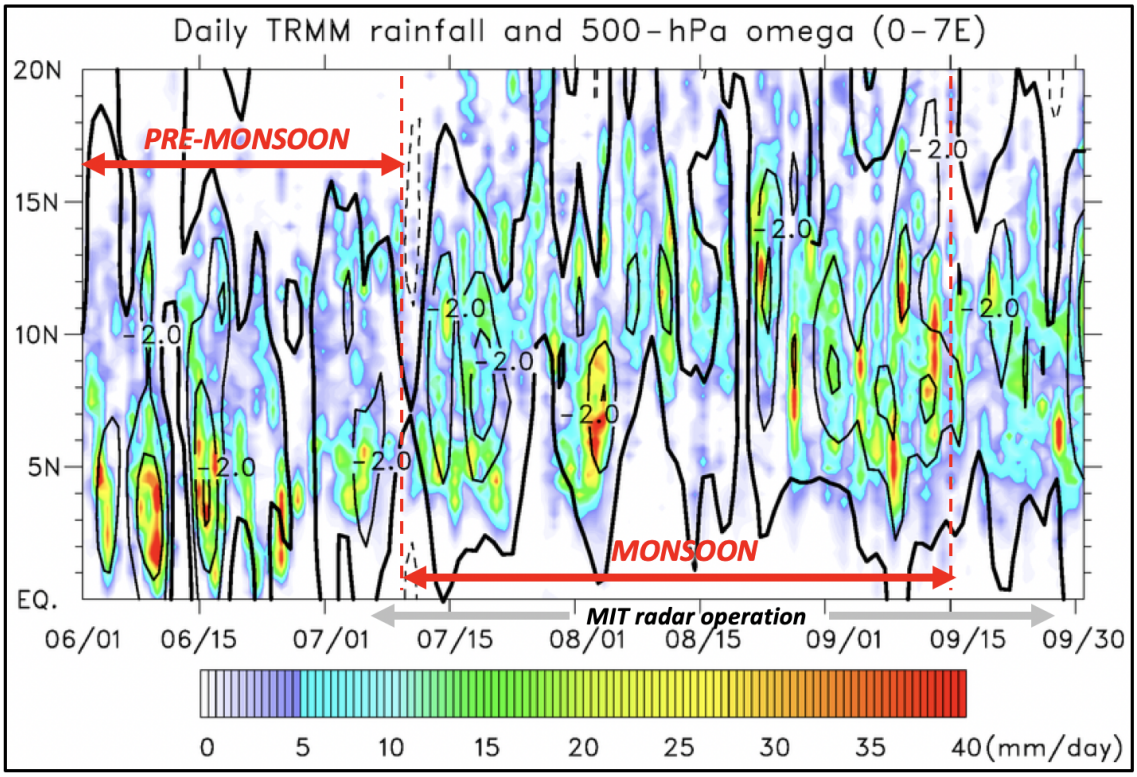

FIG. 5. June-September 2006 TRMM 3B42 rainfall (color; mm day^{-1}) from equator to 20°N over longitudes of sounding arrays (0-7°) overlain by 500-hPa vertical p-velocity (contours; hPa h^{-1}) for the period of the period of the special AMMA sounding operations. Pre-monsoon period is defined as 1 June–9 July, monsoon period 10 July–15 September. Period of MIT radar opreration indicated by gray arrows.

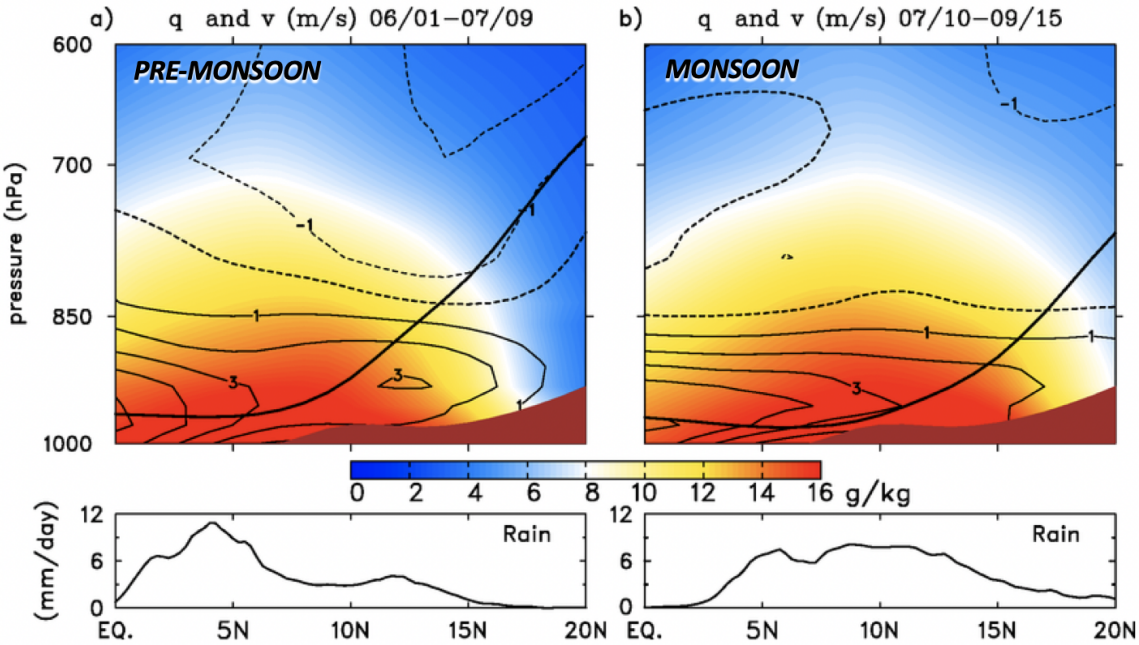

FIG. 6. North-south cross sections (equator to 20°N) averaged from 0 to 7°E of (a) pre-monsoon and (b) monsoon meridional wind (m s^{-1}, contours) and specific humidity (g kg^{-1}, color). TRMM rainfall is shown at bottom. Heavy solid lines are estimates of cloud-base height based on surface observations. Cloud base height (CBH) in km is computed as CBH = $0.125(T_s - T_d)$ from Stull (1988), where T_s is the surface temperature and T_d is the surface dew point temperature. Dark brown shaded areas denote topography.

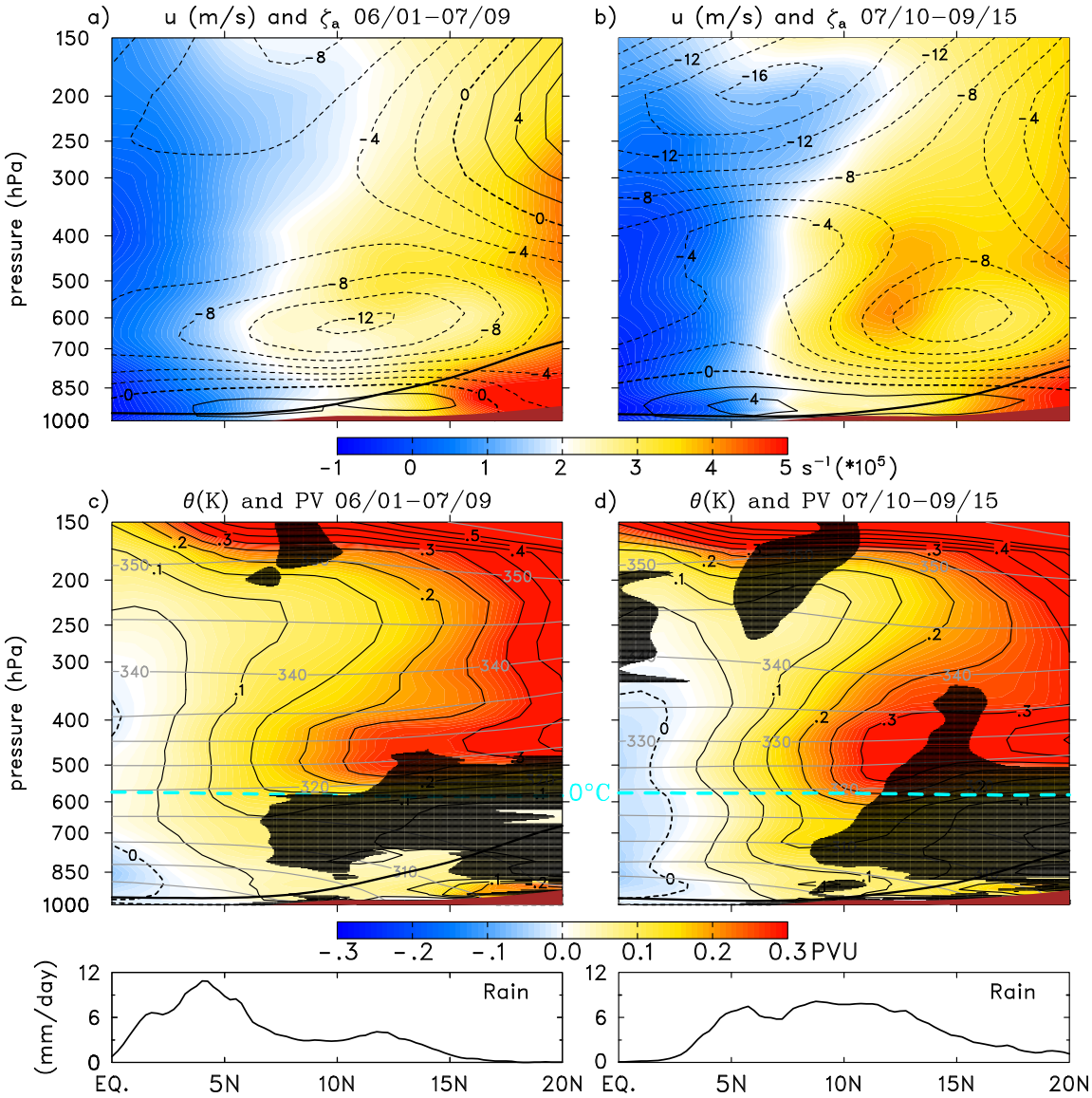

FIG. 7. North-south cross sections (equator to 20°N) averaged from 0 to 7°E of (a) pre-monsoon and (b) monsoon zonal wind (m s^{-1}, contours) and absolute vorticity ζ_a (10^{-5} s^{-1}, color), and (c) pre-monsoon and (d) monsoon potential vorticity PV (PVU = 10^{-6} K m^2 kg^{-1} s^{-1}, contoured colors) and potential temperature (K, gray solid contours). Stippled areas in (c) and (d) indicate where the north-south gradient of PV is negative. TRMM rainfall is shown at bottom. Heavy solid lines are estimates of cloud-base height based on surface observations. Dashed light blue line denotes 0°C level.

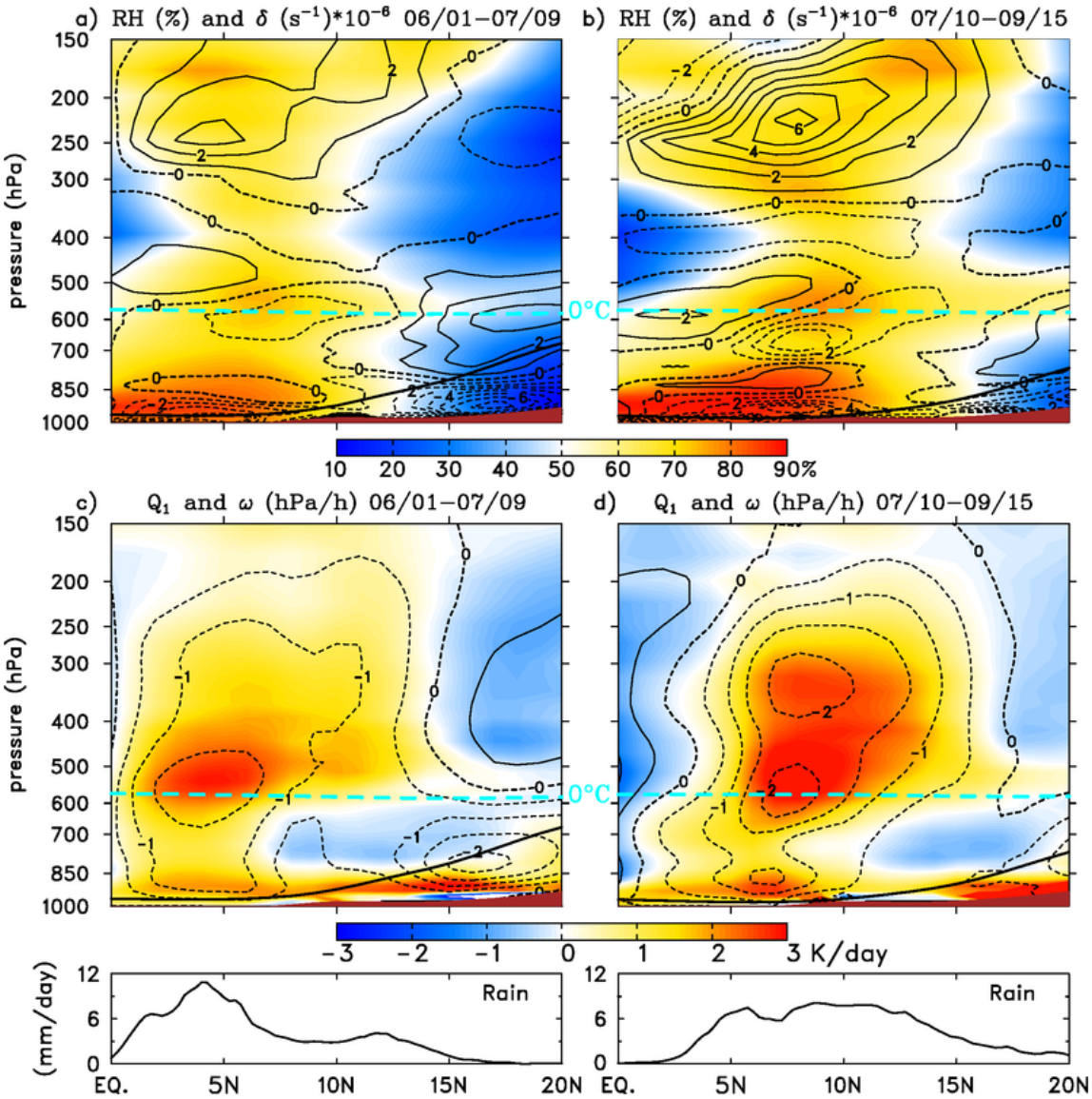

FIG. 8. North-south cross sections (equator to 20°N) averaged from 0 to 7°E before and after monsoon onset of (a) and (b) divergence 10^{-6} s^{-1}, contours) and relative humidity (%, with respect to ice for $T < 0$°C, color), and (c) and (d) apparent heat source Q_1 (K hr^{-1}, color) and vertical p-velocity ω (hPa h^{-1}, contours). Dashed cyan line marks 0°C level. TRMM rainfall is shown at bottom. Heavy solid lines are estimates of cloud-base height based on surface observations.

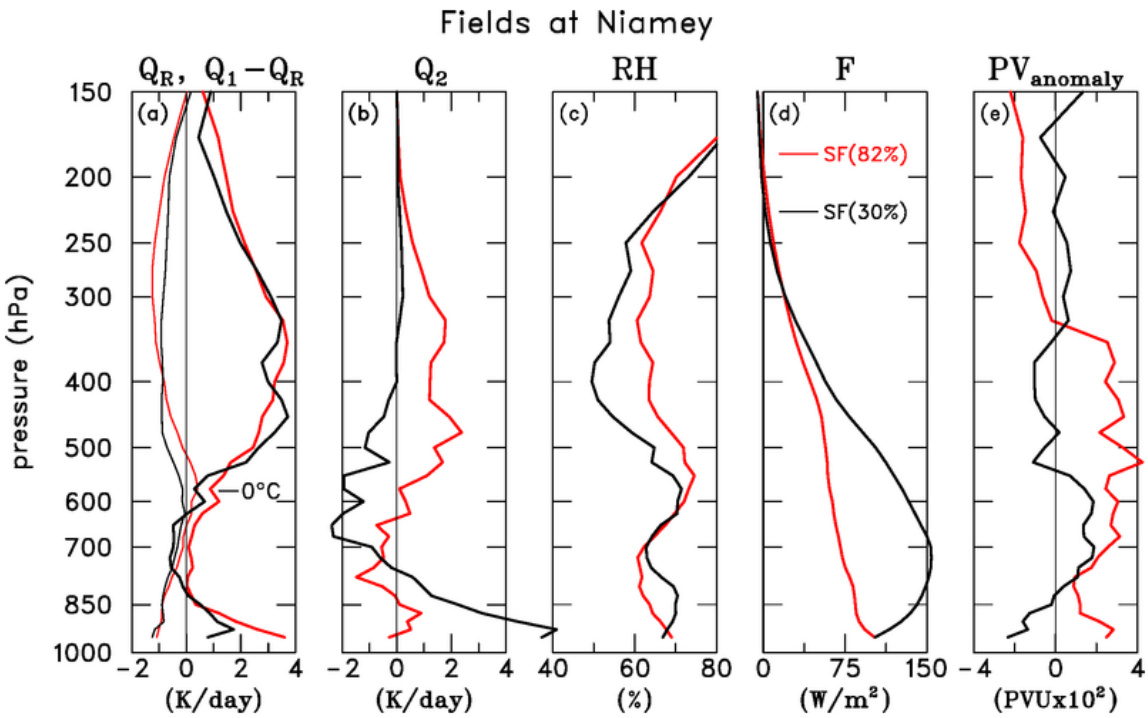

FIG. 9. Vertical profiles of (a) radiative heating rate Q_R (thin curves) and convective heat source $Q_1 - Q_R$ (thick curves) in units of K day^{-1}, (b) apparent moisture sink Q_2 (K day^{-1}), (c) relative humidity (%, with respect to ice for sub-freezing temperatures), (d) vertical eddy flux of moist static energy F (W m^{-2}), and (e) potential vorticity anomaly (PVU = 10^{-6} K m^2 kg^{-1} s^{-1}) for MIT-radar-based average stratiform fraction SF of 82% (red) and 30% (black). In other words, the red (black) curves can be considered representative of precipitation events predominantly stratiform (convective) in nature. Curves show profiles when radar times matched up with sonde times during the period when radar data were available.

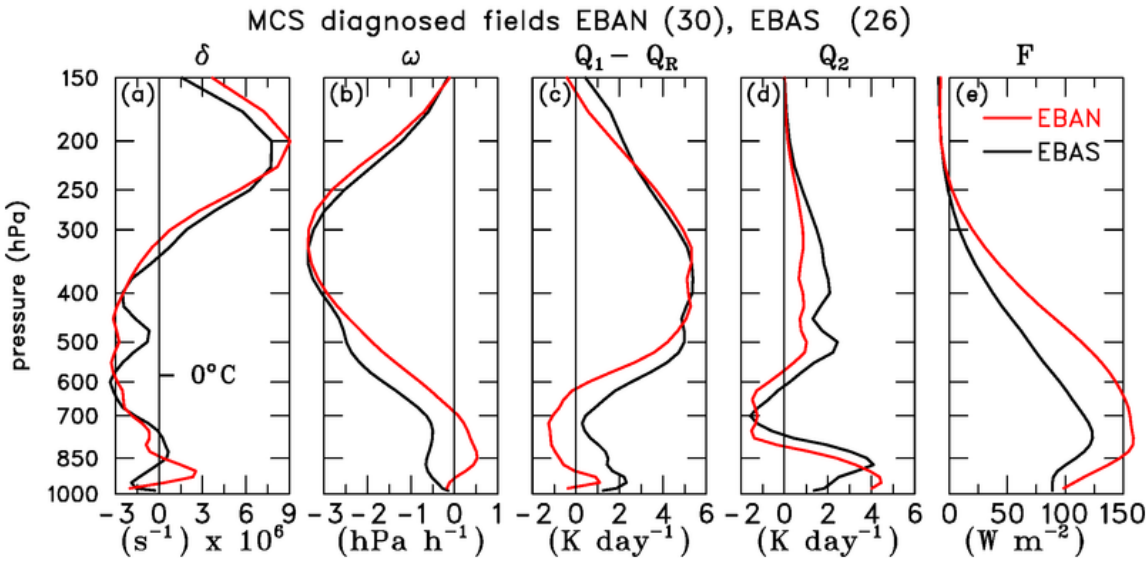

FIG. 10. Vertical profiles of (a) divergence (10^{-6} s^{-1}), (b) vertical motion (hPa h^{-1}), (c) convective heat source ($Q_1 - Q_R$; K day^{-1}), (d) apparent moisture sink Q_2 (K day^{-1}), and (e) vertical eddy flux of moist static energy F (W m^2) for squall line (MCS) passage at MIT radar site at Niamey for northerly track systems (EBAN) and southerly track systems (EBAS). Number of six-hourly sounding times used in the averages given in parentheses.

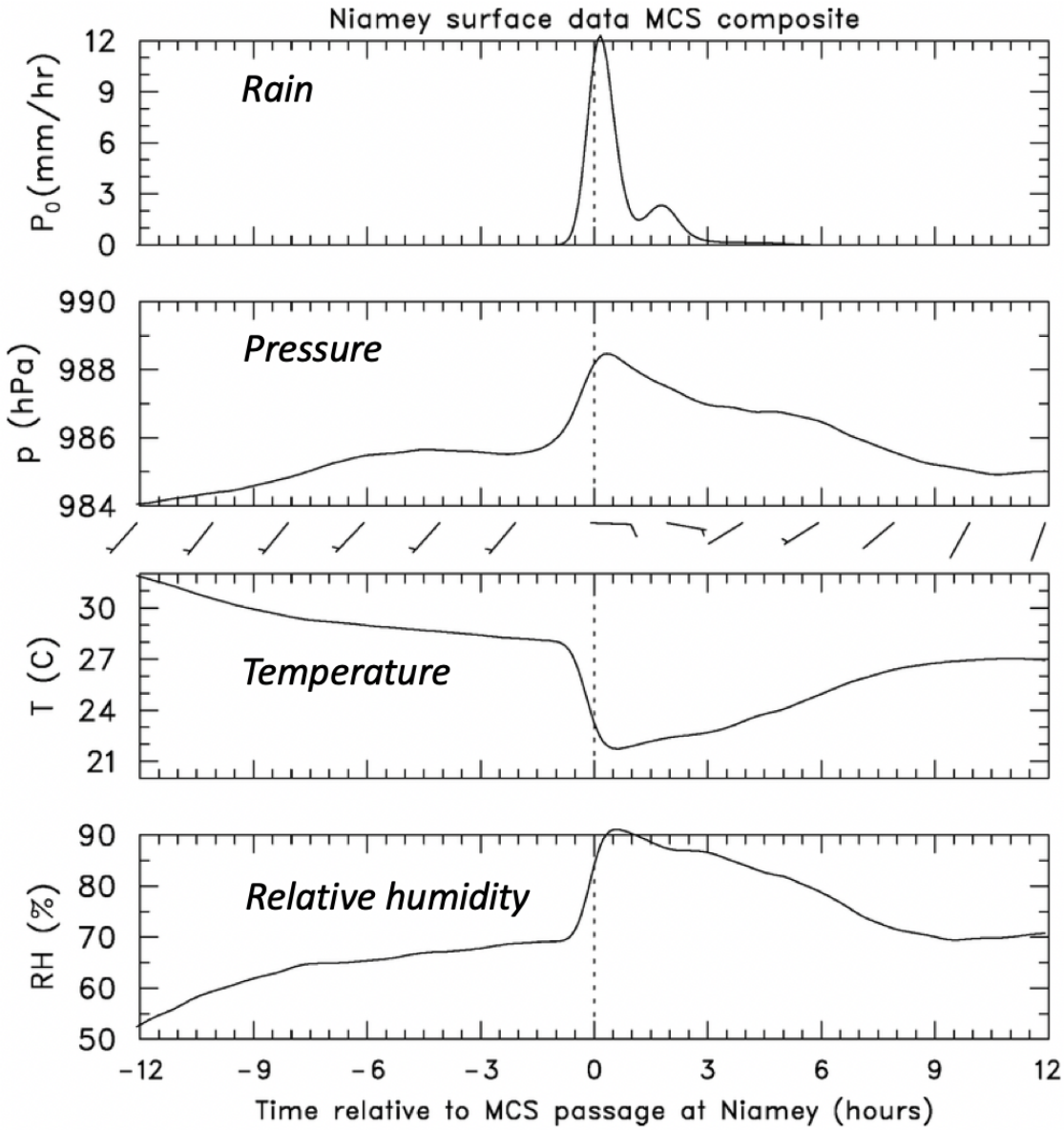

FIG. 11. (top to bottom) Time series relative to composite convective line passage of surface precipitation (mm h^{-1}), pressure (hPa), wind vectors (one full barb = 10 m s^{-1}), temperature (C), and relative humidity RH (%) at the Niamey ARM site.

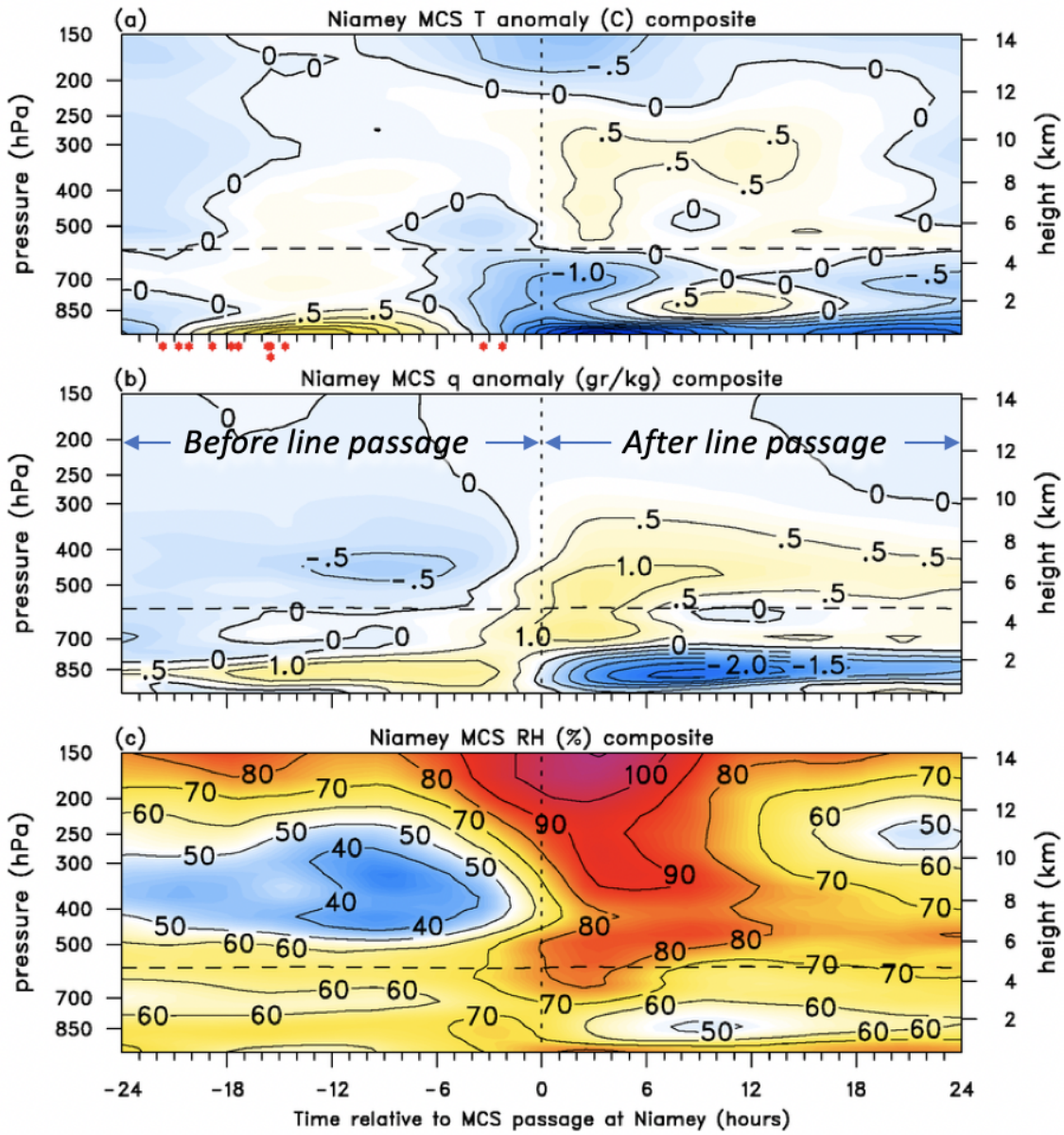

FIG. 12. Time series relative to composite convective line passage of (a) temperature anomaly (°C) and (b) specific humidity anomaly (g kg^{-1}) representing departures from monsoon period (10 July–15 September) respective means, and (c) relative humidity RH (%, with respect to ice for $T < 0$°C) at Niamey radar site. Horizontal dashed lines denote 0°C level. Red dots at base of top panel indicate the time of noon prior to squall passage for the 12 cases.

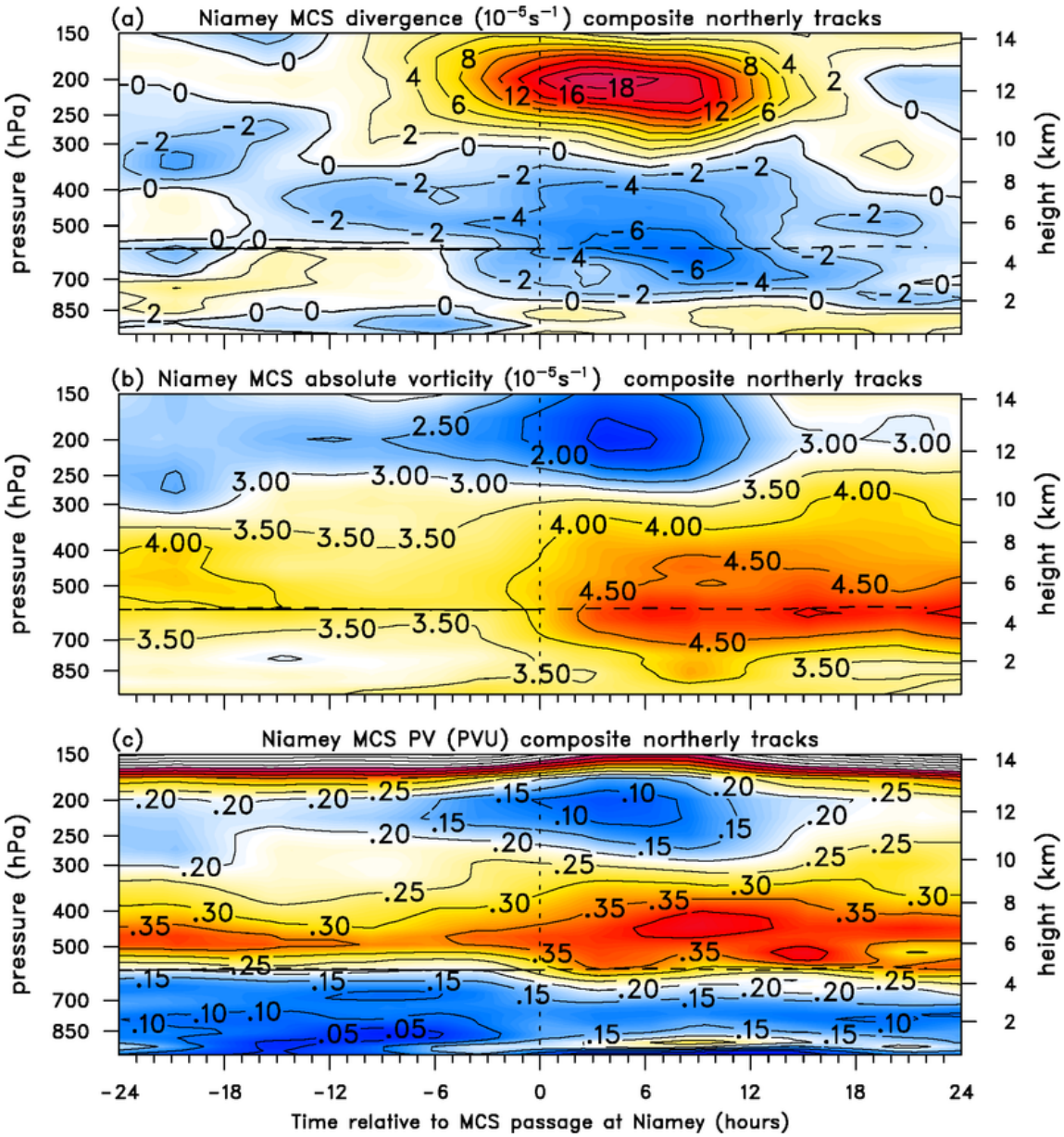

FIG. 13. Time series relative to composite convective line passage of (a) divergence (10^{-5} s^{-1}), (b) relative vorticity (10^{-5} s^{-1}), and (c) potential vorticity (PVU = 10^{-6} K m^2 kg^{-1} s^{-1}) at Niamey radar site. Horizontal dashed lines denote 0°C level.

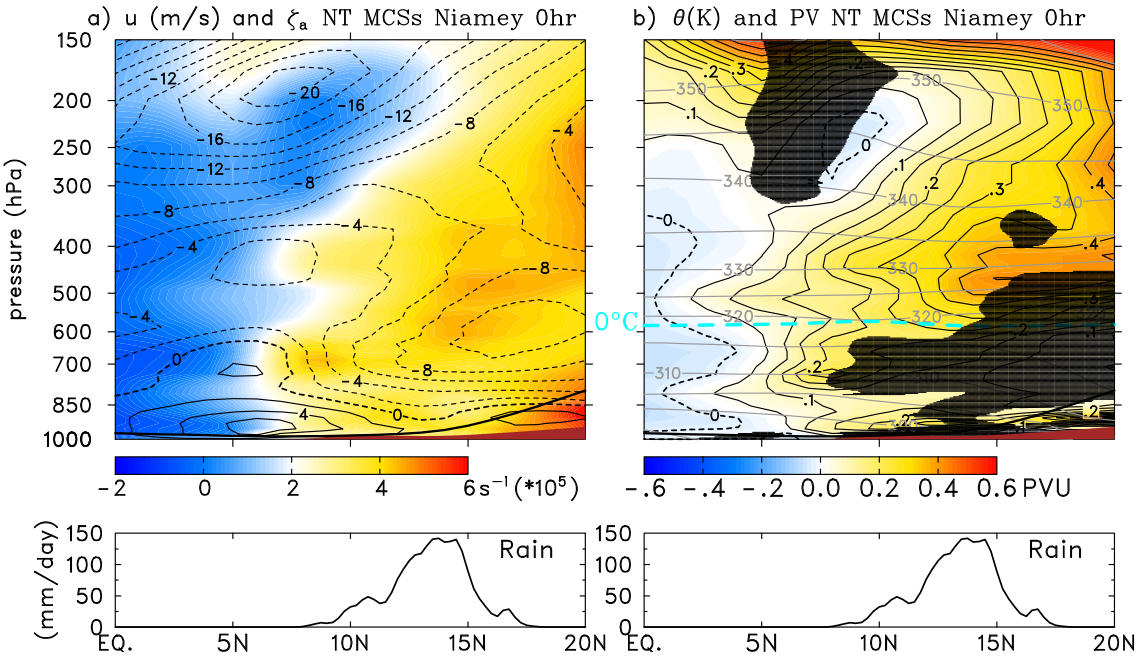

FIG. 14. North-south cross sections (equator to 20°N) averaged from 2 to 3°E of (a) zonal wind (m s^{-1}, contours) and absolute vorticity (10^{-5} s^{-1}, shading) and (b) potential temperature (K, gray contours) and potential vorticity PV (PVU = 10^{-6} K m^2 kg^{-1} s^{-1}, contoured color field) for the 7 northerly track squall line cases. Stippling indicates where the north-south gradient of PV is negative. TRMM rainfall for the same cases is shown at bottom. Heavy solid lines are estimates of cloud-base height based on surface observations. Light blue line denotes the 0°C level.

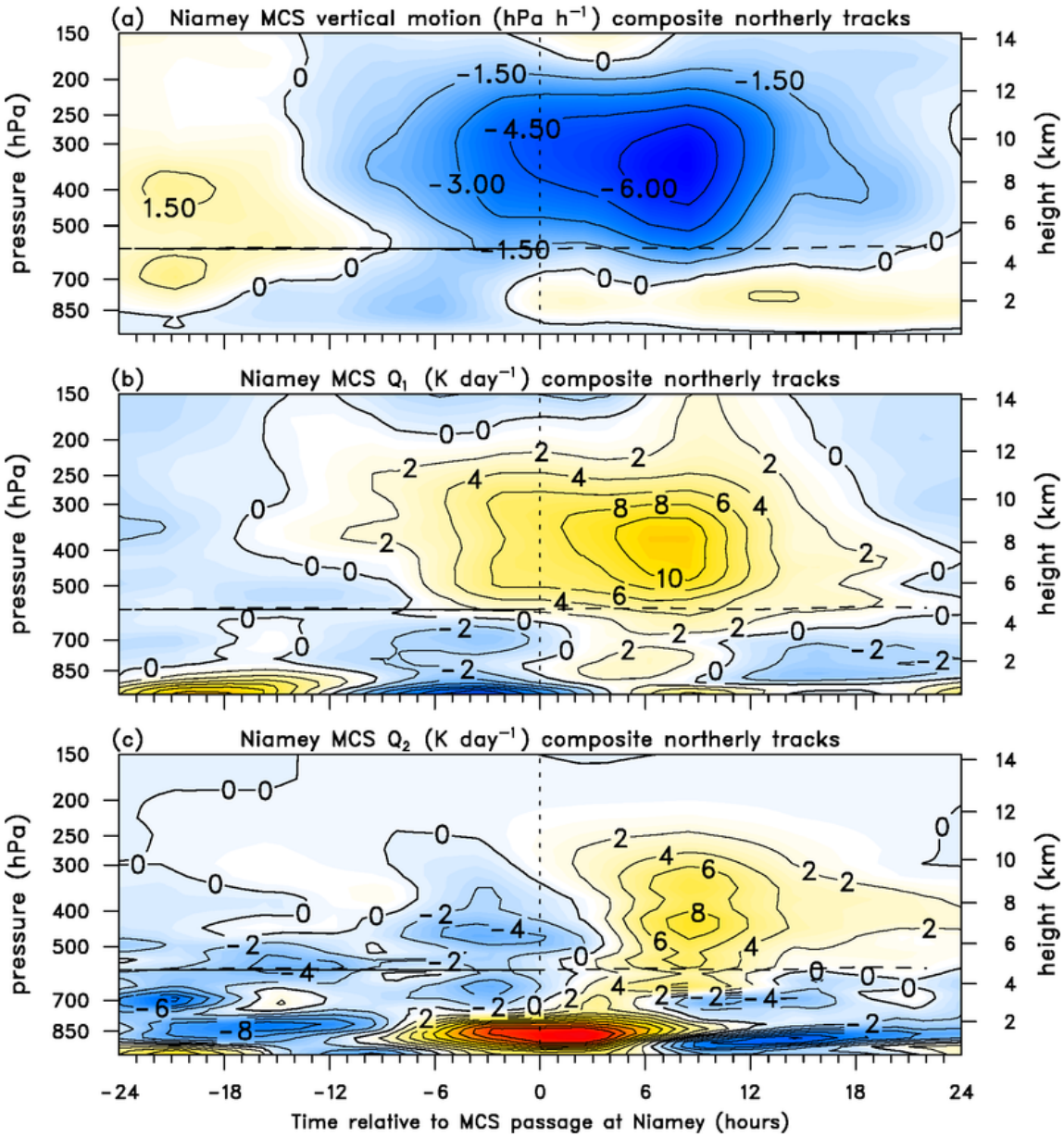

FIG. 15. Time series relative to composite convective line passage of (a) vertical motion (hPa h^{-1}), (b) apparent heat source Q_1 (K day^{-1}), and (c) apparent moisture sink Q_2 (K day^{-1}) at Niamey radar site. Horizontal dashed lines denote 0°C level.

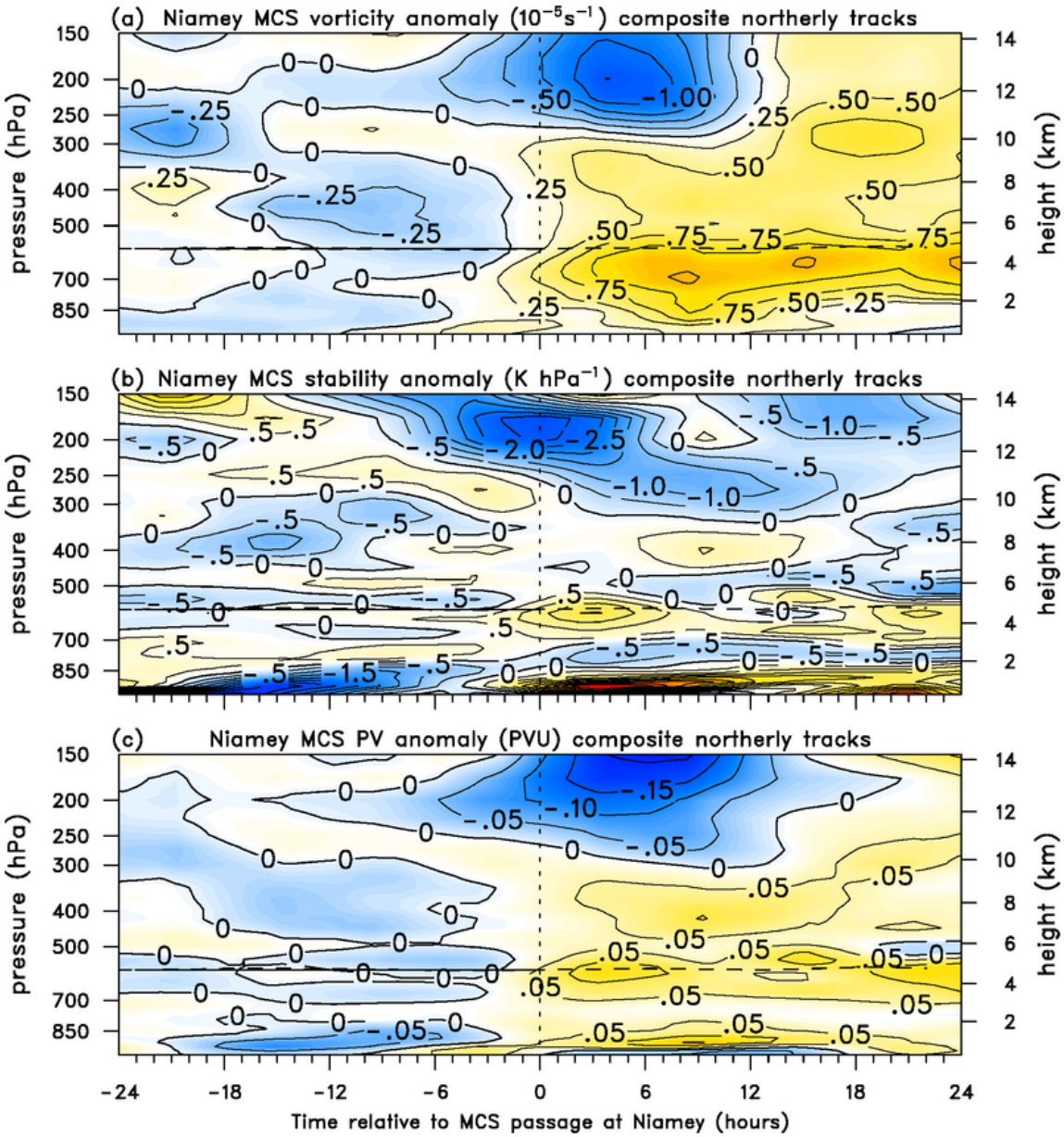

FIG. 16. Time series relative to composite convective line passage of anomalies of (a) vorticity (10^{-5} s^{-1}), (b) stability (K hPa^{-1}), and (c) potential vorticity (PVU = 10^{-6} K m^2 kg^{-1} s^{-1}) at Niamey radar site. Anomalies are relative to the monsoon period (10 July-15 September) mean fields. Horizontal dashed lines denote 0°C level.

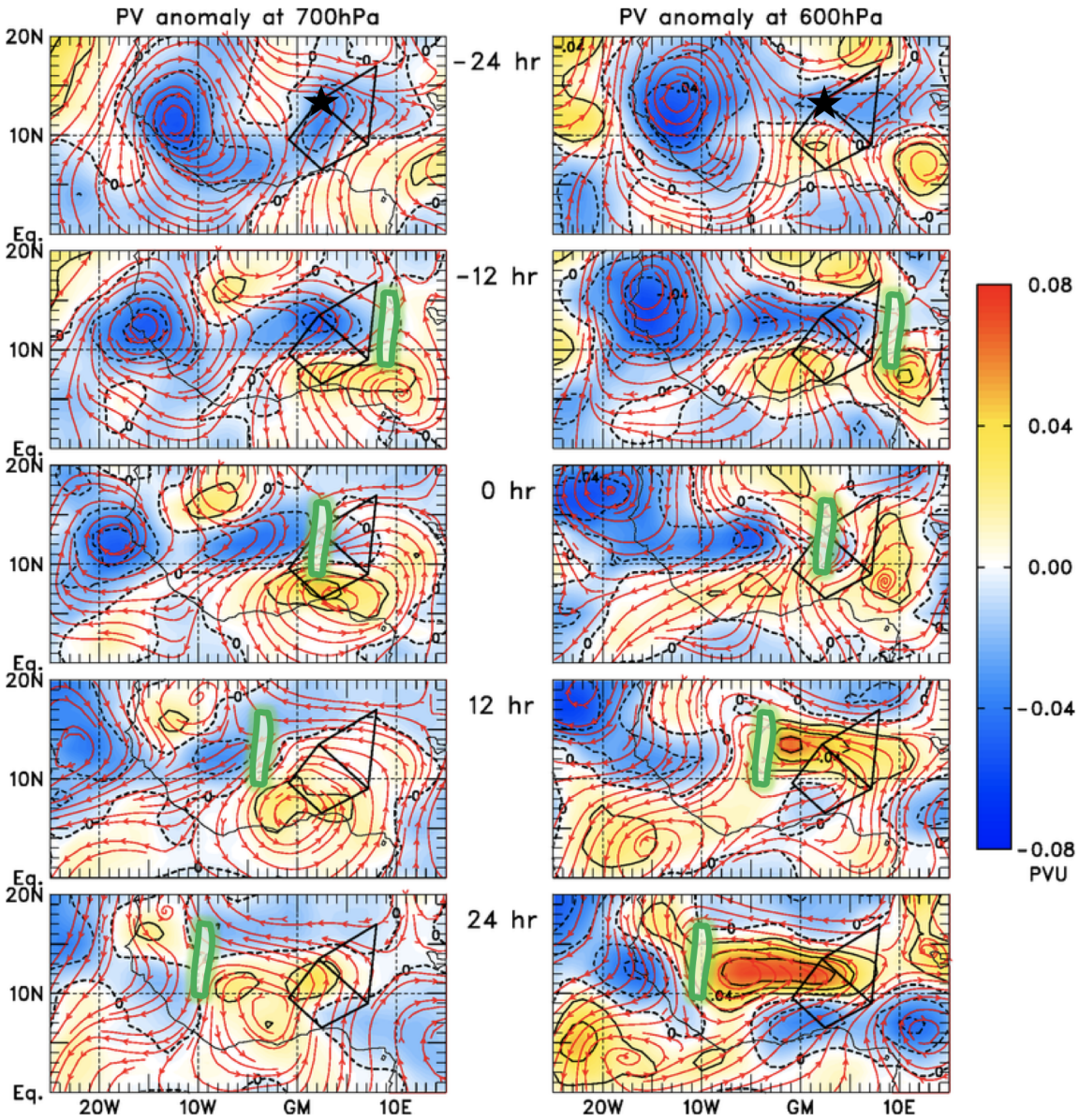

FIG. 17. Succession of composite anomaly maps of PV and streamline fields at 700 and 600 hPa from 24 hours before to 24 hours after convective line passage at MIT radar site at Niamey (marked by stars in top panels). PV units are 10^{-6} K m^2 kg^{-1} s^{-1}. The streamline and PV anomalies are relative to the monsoon period (10 July-15 September) mean fields. Green line segments denote estimated positions, orientation, and dimension of convective line based on 15 m s^{-1} west-northwestward movement, information provided in Nieto Ferreira et al. (2009), and assuming for illustrative purposes no change in structure over the period indicated. Panels on right are in proximity to the mean 0°C level (575 hPa).

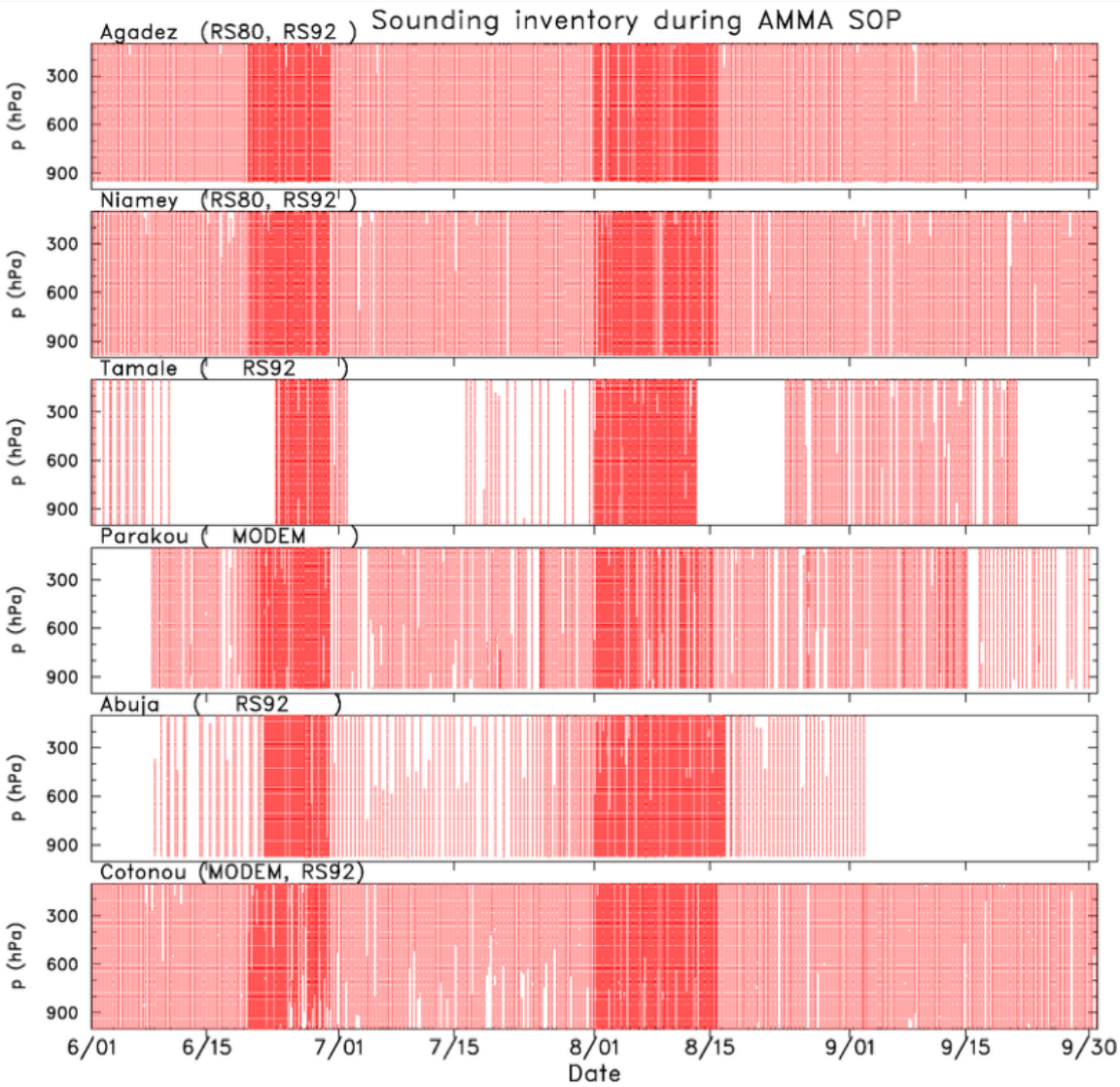

Fig. A1. Visual sounding inventory of upper-air data for six core sites. Each line of dots indicates the layer of usable data in a successful sonde launch. Denser lines in late June and early August indicate Intensive Observing Periods (IOPs) with 8/day frequency. Sonde types used at each site are shown next to site name.

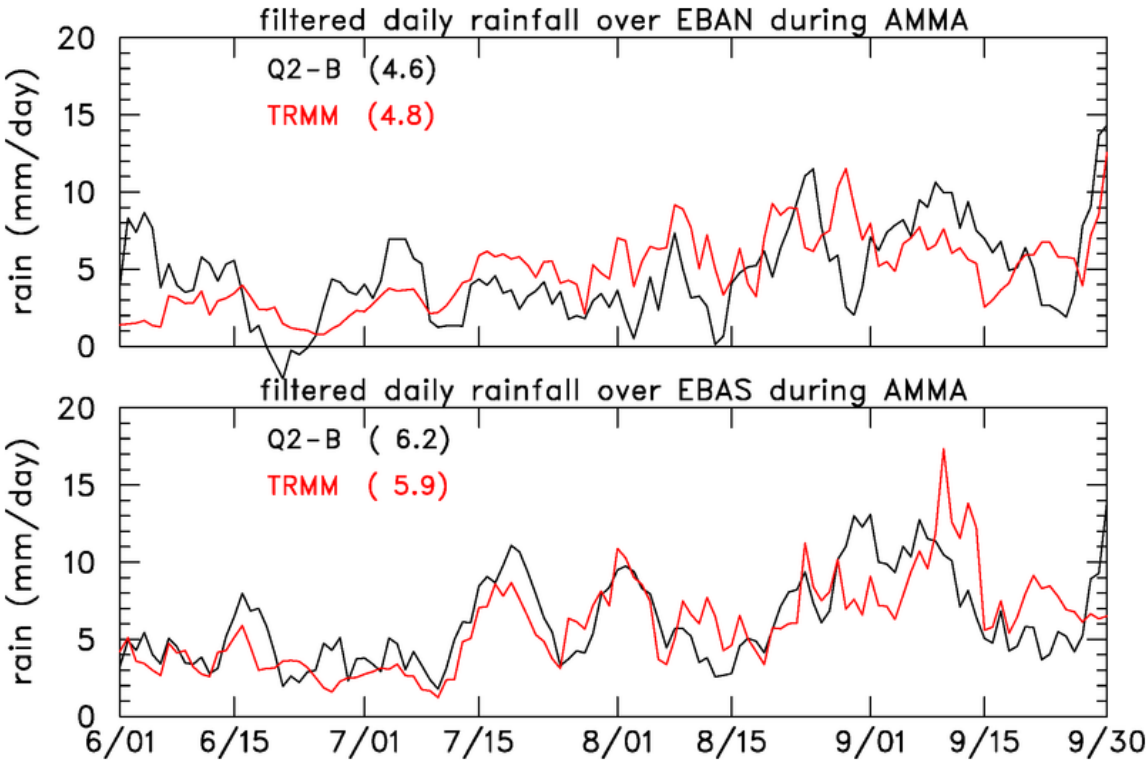

Fig. A2. Time series of five-day running mean rainfall from the moisture budget (Q2-B) and TRMM 3B42 over EBAN and EBAS for June-September 2006. Mean values (mm day^{-1}) are shown in parentheses.